AN ADJOINT-BASED OPTIMIZATION METHOD FOR GAS PRODUCTION IN SHALE RESERVOIRS

A.A. NOVOTNY, M. MURAD, AND S. LIMA

ABSTRACT. In this work we consider a new model for flow in a multiporosity shale gas reservoir constructed within the framework of an upscaling procedure where hydraulic fractures are treated as $(n-1)$ interfaces $(n=2,3)$. Within this framework the hydrodynamics is governed by a new pressure equation in the shale matrix which is treated as a homogenized porous medium composed of organic matter (kerogen aggregates with nanopores) and inorganic impermeable solid (clay, calcite, quartz) separated from each other by a network of interparticle pores of micrometer size. The solution of the pressure equation is strongly influenced by the constitutive response of the retardation parameter and effective hydraulic conductivity where the former incorporates gas adsorption/desorption in the nanopores of the kerogen. By focusing our analyses on this nonlinear diffusion equation in the domain occupied by the shale matrix, an optimization strategy seated on the adjoint sensitivity method is developed to minimize a cost-functional related to gas production in a single hydraulic fracture. The gradient of the objective functional computed with the adjoint formulation is explored to update the controlled pressure drop aiming to optimize production in a given window of time. The combination of the direct approach and gradient-based optimization using the adjoint formulation leads to the construction of optimal production scenarios under controlled pressure decline in the well. Numerical simulations illustrate the potential of the methodology proposed herein in optmizing gas production.

1. INTRODUCTION

For decades shales have been envisioned by the petroleum industry as source rocks of hydrocarbons or barriers for their movement [18, 39, 44, 45]. However, owing to the rapidly increasing demand for global oil and gas resources they have also emerged as alternative hosting hydrocarbon formations. Likewise tight-gas sands, coalbed methane, and heavy oil, shales fall in the category of unconventional reservoirs [23]. Such a terminology refers to hydrocarbon-bearing formations that generally do not produce economic flow rates unless effective stimulation techniques are adopted to enhance permeability at feasible scenarios [42]. The economic viability hinges on effective stimulations techniques to enhance production, such as advanced drilling and completion along with multi-stage hydraulic fracturing which creates complex fracture networks that connect reservoir surface area to the wellbore [23, 42].

Several macroscopic properties of shales are strongly correlated with the microstructure, which still remains poorly understood compared to conventional reservoirs. Among the complex features we may highlight the presence of multiple substructures associated with multimodal pore-size distributions; the high degree of microstructural and compositional heterogeneity, strongly correlated with the presence of distinct organic and inorganic solid phases; extremely tiny pores of nanometer size and ultra low permeability [14, 15, 16, 40]. In addition to fractures, distinct levels of pores appear associated with the gas-wet kerogen and water-wet system of nanometer to micrometer interparticle pores which provide the pathways for gas movement in the shale matrix. In such a complex microstructure, kerogen appears in the form of random scattered inclusions within the inorganic phase with percentage quantified by the total organic carbon (TOC) [1, 5]. The intraorganic nanopores within kerogen exhibit irregular, bubble-like, elliptical cross sections generally ranging between 5 and 500 nm in length in thermally mature gas shales [1]. In addition to the organic matter which plays the role of storage sites for adsorbed gas in the intra-kerogen nanopores, the inorganic solid is mainly constituted by a mixture of silicate minerals such as quartz, clays, carbonates, feldspars and pyrite [17, 30, 48]. The systems of organic and inorganic matter are separated from each other by the network of interparticle pores of size distribution ranging from nano to micrometers, usually partially saturated with water containing dissolved gas. The connectivity of the

Key words and phrases. Shale Gas Reservoir, Pressure Equation, Gas Adsorption, Gradient-Based Optimization, Adjoint-based Iterative Algorithms, Flow Sensitivity.

network of interparticle pores plays an important role in providing hydraulic conductivity for gas flow towards the network of hydraulic fractures. On the other hand, nanoporosity within the organic matter aggregates plays an essential role in gas storativity.

The behavior of the adsorbed gas in the nanopores next to the kerogen particles is usually described by the classical Langmuir isotherm, whose accuracy is restricted to the monolayer adsorption picture [28, 29, 44] where the characteristic length of the nanopores l is much higher than the diameter of the methane molecule d. In the case of ultra nanopores (e.g. $l < 5d$) more sophisticated theories have been developed to construct adsorption isotherms and compute partition coefficients. Among then we highlight Molecular Dynamics, Monte Carlo Simulation and Density Functional Theory [20, 26, 27, 29, 38, 41].

The above-mentioned microstructure description induces highly complex features in the gas hydrodynamics leading to the appearance of several coupled phenomena such as adsorption/desorption, anomalous behavior of the gas in the nanopores gas dissolution in the water phase in the interparticle pores, Knudsen slip flow and mass exchange between matrix and fracture flows [11, 32, 40]. The homogenization of the single phase gas flow in the interparticle pores gives rise to a nonlinear parabolic equation posed in the domain occupied by the matrix which macroscopically represents a medium of three-coexisting phases associated with the kerogen aggregates (kerogen particles and adsorbed gas in the intra-organic nanoscopic pores) along with the interparticle pores partially saturated by free gas and an aqueous solution with dissolved gas and impermeable inorganic matter [28, 29]. The quantification of the relative roles of each phenomenon involved gives rise to significative challenges in modeling and optimization issues associated with methane production in unconventional reservoirs. More specifically, the constitutive laws underlying the retardation coefficient and hydraulic conductivity which appear in the nonlinear diffusion equation shall be capable of capturing the local features and need to be rigorously reconstructed by upscaling the microscopic description [1, 2, 25, 34].

Historically, theories for single phase gas flow in a multiporosity shale system have emerged from the well established frameworks of dual and triple porosity/permeability models [34, 46, 49]. Such a class of multiporosity models, extended in [36] to the fully compressible case, has been the cornerstone for incorporating the aforementioned reactive transport phenomena in shale taking place at distinct spatial and temporal scales. Such phenomena bring severe nonlinearities to the diffusion equation where the upscaled coefficients shall incorporate a variety of local phenomena such as local gas adsorption in nanopores [28, 29], higher apparent permeability induced by Knudsen diffusion and slippage mechanism at the pore wall [25], classical Fickian diffusion of the dissolved gas in the water phase [24] and Darcy-Forchheimer flow in high fracture permeable systems [19].

Despite the aforementioned substantial advances, the rigorous bridging between the local pore-scale microscopic physics and the constitutive response of the retardation coefficient in the nonlinear diffusion equation governing gas movement in the matrix was recently constructed in [28, 29]. Among other features, we particularly highlight the accurate numerical reconstruction of the dependence of this parameter on TOC, clay content, porosities and gas pressure. Application of this two-scale approach gives rise to a new nonlinear pressure equation (see [28] for details) which will be explored herein as the bases of the forward problem for the subsequent optimization strategy.

Throughout the manuscript our forward and optimization methodologies shall focus on gas flow in the matrix. Thus, we adopt a time-scale assumption considering fast gas flow in the fractures compared to the hydrodynamics in the matrix so that the controlled pressure in the well is transferred instantaneously to the fractures which play the role of imposing Dirichlet boundary condition for flow in the matrix. In this context, our forward problem is fully characterized by the new pressure equation with complex constitutive laws underlying the retardation and conductivity coefficients whose magnitude revolve around the local behavior of the microstructure [28, 29]. In this scenario, we proceed beyond the numerical solution of the forward model and strive to strike the construction of optimal controlled pressure protocols and exploitation strategies capable of maximizing gas production for a given window of time.

Over the past few decades, a variety of computational algorithms has been developed for solving constrained nonlinear optimal control problems [4]. The increasingly powerful high-performance computational resources in conjunction with the development of sophisticated numerical algorithms have enabled the solution of large-scale, high-fidelity optimization problems. Some of the methodologies

developed are based on adjoint-based sensitivity methods which allows to maximize or minimize an objective functional [31]. The Fréchet–type derivatives are then used to obtain a direction of improvement of the objective function and a descent method is adopted for gradient-based optimization. Such a procedure is repeated until an extreme is eventually reached for a given convergence criterion. The resulting formulation consists in solving the forward and adjoint problems along with computing the gradient of the objective functional. Once the gradients have been obtained, a wide variety of gradient-based techniques is available to iterate towards the optimal solution; see e.g. Gill et al. [21].

In this work, we develop a new formulation for optimal gas withdrawal in unconventional shale reservoirs that combines a new forward model with efficient optimal control and model-updating algorithms for real-time production optimization to construct optimum production scenarios. The construction of the optimal methane withdrawal strategy in unconventional formations is achieved with the aid of the optimal control theory. The optimization loop is performed over the next control step and the process repeated over the lifetime of the reservoir. By postulating a general form for the objective function later identified with the net present value (NPV), we proceed by constructing accurate representations for the coefficients of the adjoint equations in terms of the retardation coefficient, micro/nano porosities and the TOC of the shale formation. By discretizing the forward and adjoint problems by the Galerkin method and computing the derivative within a post-processing approach, numerical simulations illustrate the effect of the different pressure protocols on the objective function. Numerical results show the evolution of the profiles with the iteration loop towards the minimum and illustrate the robustness of the methodology proposed herein to improve gas production in NPV unconventional reservoirs.

2. Statement of the Problem

Consider the shale gas reservoir a porous medium with inorganic matter mainly composed of clay particles (kaolinite and illite) along with quartz/calcite and an organic solid composed of kerogen particles and nanopores forming the organic aggregates (Fig. 1). The gas-wet organic aggregates are filled by adsorbed methane lying in the nanopores whereas the inorganic matter is treated as a non-reactive impermeable medium for gas flow. The kerogen aggregates and inorganic matters are separated from each other by a permeable system of interparticle pores partially filled by an aqueous solution (with dissolved gas) and a free gas phase. In addition to the two levels of porosity associated with the interparticle pores and intra-kerogen aggregates, a distinct level of hydraulic fractures is present. For the sake of simplicity, we consider interparticle pores of micrometer size so that the Knudsen number is small $K_n = \mathcal{O}(10^{-3})$ [32, 40] leading to the continuum regime of free gas flow ruled by the classical form of Darcy's law. In this microstructural portrait, three distinct length scales naturally appear (Fig. 1). The nanoscale of characteristic length of $\mathcal{O}(10^{-9}m)$, where kerogen particles and nanopores are viewed as distinct phases: the microscale, with length of $\mathcal{O}(10^{-6}m)$, with nanopores and kerogen treated as overlaying continua forming the organic aggregates, distinct from the system of interparticle pores and inorganic phase: the macroscale with characteristic length of $\mathcal{O}(10^{-3}m)$ where both organic and inorganic matters along with interparticle pores are homogenized forming the natural shale matrix adjacent to the hydraulic fractures network. This latter structure is composed of lower dimension objects that separate the matrix into distinct geologic blocks.

In the process of fluid withdrawal, gas desorption from the kerogen takes place and movement occurs in the system of interparticle pores induced by Fickian diffusion of the dissolved gas and Darcy flow of the free gas. The percentage of water produced from the interparticle pores is very small and will be neglected herein. Thus, we consider immobile bound water phase lying in the interparticle pores with strong wettability to the clay. Following [28] assume that the time scale of the mass exchange between water and gas phases is fast compared to that of transport so that local thermodynamic equilibrium between free, dissolved and adsorbed gas is locally enforced.

In the developments that follow, we begin by presenting the preliminary model for flow in a rigid shale matrix by assigning a much higher stiffness to it compared to that in the hydraulic fractures. Furthermore, after presenting the results related to optimization we discuss the steps toward the inclusion of poroelastic effects.

2.1. **Hydrodynamics.**

For the sake of completeness, we begin by describing the macroscopic governing equations describing methane flow in the shale matrix. We present the developments for constructing the

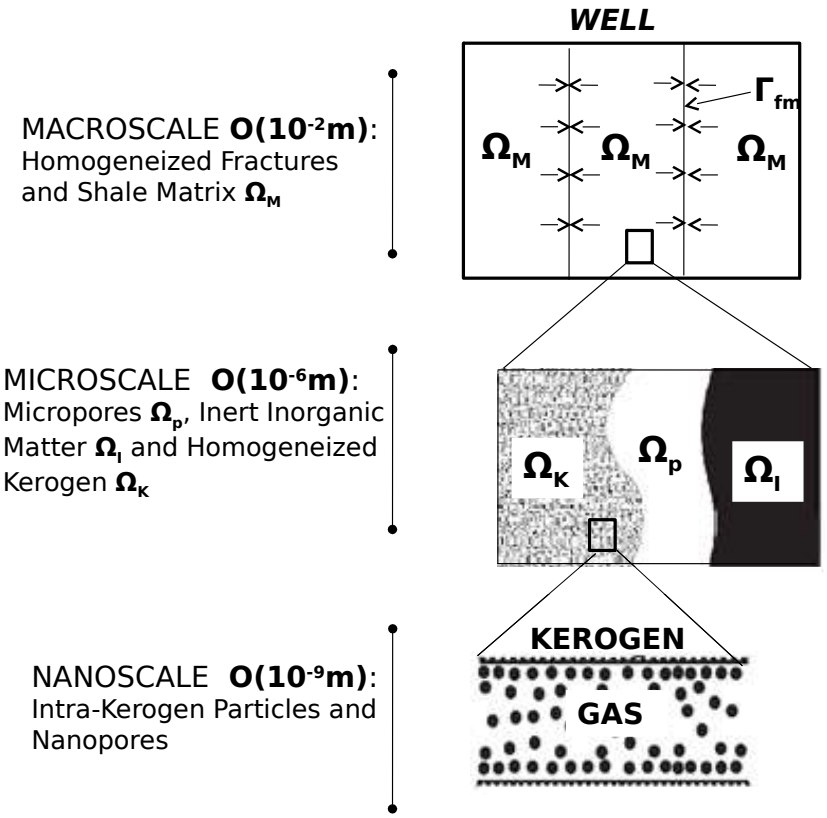

FIGURE 1. Multiscale portrait of a shale gas formation.

pressure equation characterized by the nonlinear parabolic problem. In the network of interparticle pores, free gas and the aqueous phase with dissolved gas are treated as a homogeneous mixture where Fickian diffusion of dissolved gas and flow of free gas ruled by Darcy's law take place simultaneously. After averaging to the macroscale the fluid phases along with the organic and inorganic solids are treated as superimposed continua with the hydrodynamics of gas ruled by the pressure equation.

Let $\Omega_s \subset \mathbb{R}^3$ be the domain occupied by the homogenized system of interparticle pores, kerogen aggregates and inorganic matter (shale matrix) and let t be the characteristic time scale of the flow. Mass conservation of the bulk gas reads as [28]

$$\frac{\partial m}{\partial t} + \nabla \cdot \boldsymbol{J}_b = 0 \qquad \text{in} \quad \Omega_s \times (0,T), \tag{2.1}$$

where $T \in \mathbb{R}$ is the final time, $\boldsymbol{J}_b$ the mass flux and $m = \rho\,\phi$ the total gas content in the matrix with ρ and ϕ the density and porosity respectively. Denoting P_b the pressure of the bulk gas in the interparticle pores the constitutive law for m is given by $m = R(P_b)P_b$ where $R(P_b)$ is the retardation parameter which incorporates the storativities of free, dissolved and adsorbed gas. We then have

$$\frac{\partial}{\partial t}\left(R(P_b)\,P_b\right) + \nabla \cdot \boldsymbol{J}_b = 0 \qquad \text{in} \quad \Omega_s \times (0,T). \tag{2.2}$$

In the sequel, we proceed by developing the underlying constitutive relation for the retardation coefficient R. Let φ_P, φ_I, φ_K be the volume fractions of the interparticle pores, inorganic matter and kerogen aggregates embedded in the shale matrix respectively and denote S_w the time independent water saturation in the unsaturated interparticle pores. The total gas content and retardation coefficient can be decomposed in the form [28]

$$m_s = m_d + m_b + m_a \quad \text{and} \quad R = R_d + R_b + R_a, \tag{2.3}$$

where the components $\{m_d, R_d\}$, $\{m_b, R_b\}$ and $\{m_a, R_a\}$ designate the contents of dissolved, free and adsorbed gas in the interparticle pores respectively. In what follows, we begin by deriving the

representation for R_d. To this end, denote f_l and f_b the fugacities of dissolved and free gas where the local equilibrium assumption gives $f_l = f_b$. Assuming the validity of Henry's law we have for the dissolved gas [35]

$$f_l = \frac{\mathcal{H}(P_b)\, C_l}{\rho_l}, \tag{2.4}$$

with C_l the gas concentration in the water phase, ρ_l the density of the liquid and $\mathcal{H}(P_b)$ given by Henry's law [35]

$$\mathcal{H}(P) = \mathcal{H}^* \exp\left[v^\infty \left(\frac{P - P^S}{R_g\, T}\right)\right], \tag{2.5}$$

where $\mathcal{H}^*$ denotes the Henry constant, P^S the saturation pressure of the water and v^∞ the partial molar volume at infinite dilution of methane in the liquid.

For the free gas in the micropores we have $f_b = \gamma(P_b)P_b$ where $\gamma(P_b)$ is the fugacity coefficient given by

$$\gamma(P) = \exp\left(\int_0^P \frac{Z(P') - 1}{P'} dP'\right). \tag{2.6}$$

with Z the compressibility factor. Thus, with the above-mentioned definitions the equality between fugacities furnish

$$C_l = \frac{\gamma(P_b)\, \rho_l}{\mathcal{H}} P_b, \tag{2.7}$$

which together with the representation $m_d = C_l \varphi_P S_w$ gives

$$R_d = \frac{m_d}{P_b} = \varphi_P S_w \frac{\gamma(P_b)\, \rho_l}{\mathcal{H}(P_b)}. \tag{2.8}$$

We now turn to the constitutive law for R_b. In terms of the bulk gas density ρ_b we have

$$m_b = (1 - S_w)\varphi_P \rho_b. \tag{2.9}$$

By postulating an equation of state in the form

$$\rho_b = \frac{M_m\, P_b}{R_g\, T\, Z}, \tag{2.10}$$

where R_g is the universal gas constant, T the temperature and M_m the molar mass of the gas, in a similar fashion we have for the free gas

$$R_b = \frac{m_b}{P_b} = \varphi_P \frac{(1 - S_w)}{\widetilde{Z}(P_b)}. \tag{2.11}$$

with $\widetilde{Z}(P_b) = R_g\, T\, Z / M_m$. The last component R_a in (2.3) quantifies the amount of adsorbed gas in the kerogen. Such a contribution can be computed by invoking the constitutive law of the partition coefficient G, defined as the ratio between the mean adsorbed ρ_a and the bulk gas densities

$$G := \frac{\rho_a}{\rho_b}. \tag{2.12}$$

In a similar fashion, denoting ϕ_N the intrakerogen nanoporosity we have

$$R_a = \frac{m_a}{P_b} = \frac{\rho_a \phi_N \varphi_K}{P_b} = \frac{G \rho_b \phi_N \varphi_K}{P_b} = \frac{G \phi_N \varphi_K}{\widetilde{Z}(P_b)}. \tag{2.13}$$

In order to compute G, the local gas density profiles in the organic nanopores need to be precisely reconstructed. Such task can be accomplished within the framework of the Density Functional Theory (DFT) under the assumption of local equilibrium between adsorbed and free gas (see [28] for details) or alternatively by invoking the Langmuir adsorption isotherm. Such a local time-scale assumption revolves around the estimates presented in Le et al.[29] (appendix 2) who observed high contrast between the

time scales of the flows in nano and micro pores by computing large values for the ratio between them, consequently validating thermodynamic equilibrium. Under this quasi-steady regime transients effects within the nanopores and pressure boundary layers reported in Monteiro et al. [33] can be neglected.

Within the framework of Langmuir adsorption, the adsorbed gas content per unit area of the solid surface, Γ_L, is given by [43, 45]

$$\Gamma_L = \Gamma^*_{max} \frac{P_b}{P_b + P_L}, \tag{2.14}$$

where $\Gamma^*_{max} = \Gamma_{max}/N_A$, with Γ_{max} the number of sites available for adsorption, N_A the Avogadro's number and P_L the Langmuir pressure, whose value corresponds to one-half of the maximum storage capacity. In the case of slit nanopores the mean adsorbed gas density ρ_a can be directly computed by averaging the gas content. We then have a boundary layer adjacent to the surface together with the free gas behavior lying in the interior organic pores (see [28] for details)

$$\rho_a = \frac{1}{H/2}\left(\int_{d/2}^{d} \frac{\Gamma_L}{d} dz + \int_{d}^{H/2} \rho_b dz\right) = \frac{1}{H}\left[\Gamma_L + \rho_b(H - 2d)\right], \tag{2.15}$$

where H is the separation distance between the parallel organic solid particles and d the diameter of the gas molecules. Inserting (2.10), (2.14) and (2.15) in (2.12) we obtain for slit pores

$$G = \frac{1}{H}\left(\frac{\Gamma^*_{max}\widetilde{Z}}{P_b + P_L}\right) + \frac{H - 2d}{H}. \tag{2.16}$$

Its worth noting that the representation (2.13) for the retardation coefficient can be rewritten in terms of the TOC$= M_K/(M_K + M_I)$ with M_K and M_I the mass of kerogen and inorganic matter, respectively. By designating ρ_K and ρ_I the densities of kerogen and inorganic matter respectively, a simple calculation allows to replace φ_K by TOC in the form (see Appendix A for details)

$$\varphi_K = 1 - \varphi_P - \varphi_I = \frac{(1 - \varphi_P)}{1 + \dfrac{\rho_K(1 - TOC)(1 - \phi_N)}{\rho_I\, TOC}}, \tag{2.17}$$

which when combined with (2.3), (2.8) , (2.11) and (2.13) gives

$$R(P_b) = \varphi_P\left[S_w \frac{\gamma(P_b)\,\rho_l}{\mathcal{H}(P_b)} + \frac{(1 - S_w)}{\widetilde{Z}(P_b)}\right] + \frac{(1 - \varphi_P)}{1 + \dfrac{\rho_k(1 - TOC)(1 - \phi_N)}{\rho_I\, TOC}} \frac{\phi_N G}{\widetilde{Z}(P_b)}. \tag{2.18}$$

For the complete derivation of the pressure equation it remains to postulate Darcy's law for the mass flux in (2.1). Denoting $\boldsymbol{K}_b^{eff}$ the effective conductivity neglecting gravitational effects we have

$$\boldsymbol{J}_b = -\boldsymbol{K}_b^{eff} \nabla P_b, \tag{2.19}$$

It should be noted that the average conductivity exhibits two contributions: the first stems from the hydraulic conductivity of free gas

$$\boldsymbol{k}_b^{eff} = \rho_b \varphi_P \frac{\boldsymbol{k}_b\, k_r}{\mu_g} T(\varphi_P), \tag{2.20}$$

with $\boldsymbol{k}_b$ and $k_r(S_w)$ the absolute and relative permeabilities, μ_g the viscosity of the gas and $T(\varphi_P)$ the tortuosity function associated with the interparticle pores. In addition, the mean diffusion coefficient $D_l(S_w)$ associated with the movement of dissolved methane in the water phase is given by

$$\boldsymbol{D}^{eff} = \varphi_P\, D_l(S_w)\, \widetilde{g}(P_b)\, T(\varphi_P), \quad \widetilde{g}(P_b) = \frac{dC_l}{dP_b} = \frac{d}{dP_b}\left(\frac{\gamma(P_b)\rho_l}{H(P_b)} P_b\right), \tag{2.21}$$

where C_l is the methane concentration in the water phase given in (2.7). Thus, the effective conductivity for free and dissolved gas can be represented in the form

$$\boldsymbol{K}_b^{eff} = \boldsymbol{k}_b^{eff} + \boldsymbol{D}^{eff} = \varphi_P\left(\rho_b \frac{\boldsymbol{k}_b\, k_r}{\mu_g} + \widetilde{g}(P_b) D_l(S_w)\right) T(\varphi_P). \tag{2.22}$$

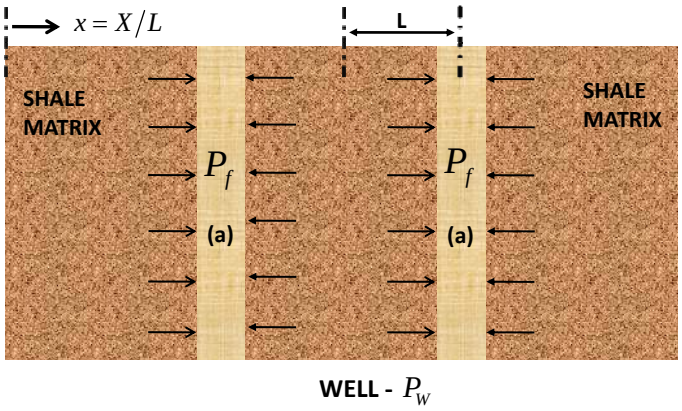

FIGURE 2. Well–ordered arrangement of parallel equally spaced hydraulic fractures orthogonal to a horizontal well.

2.2. **Reduced Case.** We shall henceforth present our optimization strategy in the case of gas withdrawal from a homogeneous shale matrix surrounded by a well ordered parallel arrangement of hydraulic fractures orthogonal to a horizontal well (Fig. 2). Such an arrangement is characterized by the absence of cross flow and consequently the nonlinear parabolic model reduces to an one-dimensional equation along the coordinate x orthogonal to the fractures and parallel to the well (Fig. 2). Owing to the simpler manipulations involved, we select the formulation posed in terms of the density of the bulk gas in the interparticle pores rather than pressure. Thus, in what follows we rewrite the pressure equation in terms of the density $\rho(x,t) := \rho_b(x,t)$ which hereafter will be treated as the main variable for the construction of the objective function. Let $p_f(t)$ be the prescribed pressure at the matrix/fracture interface which, under our time scale assumption, is equal to the well pressure $p_w(t)$. Further let $\rho_f(t)$ be the controlled density computed from the equation of state (2.10) with $p = p_f$ for a given constant temperature. In order to rephrase the problem in terms of the density, we rewrite Darcy's law and the constitutive relation for the retardation coefficient in terms of $\rho(x,t)$. Exploring symmetry in the center of two adjacent hydraulic fractures in the well ordered arrangement of Fig. 2, our one-dimensional nonlinear diffusion problem for $\rho = \rho(x,t)$ in $0 < x < 1$ and $0 < t < T$ reads as

$$\begin{cases} (R\rho)_t(x,t) - (K^\star \rho_x)_x(x,t) &= 0\,, \\ \rho(0,t) &= \rho_f(t)\,, \\ K^\star \rho_x(1,t) &= 0\,, \\ \rho(x,0) &= \rho_0(x)\,, \end{cases} \tag{2.23}$$

with $x = X/L$ a dimensionless spatial coordinate, $\rho_0(x)$ the initial condition and $R = R(\rho(x,t))$ the retardation coefficient now represented in terms of density in the form

$$R(\rho) = \varphi_P(1-S_w) + \varphi_P S_w \rho_l RT \frac{Z(\rho)\gamma(\rho)}{\mathcal{H}(\rho)} + \frac{(1-\varphi_P)}{1 + \dfrac{\rho_k(1-TOC)(1-\phi_N)}{\rho_I\, TOC}} \phi_N G(\rho). \tag{2.24}$$

In addition, in terms of density the effective conductivity $K^\star = K^\star(\rho(x,t))$ in the x–coordinate can be represented as

$$K^\star(\rho) = k_b^{eff} + D^{eff} \tag{2.25}$$

with

$$D^{eff} = \varphi_P\, D_l(S_w)\, \widetilde{g}(P_b)\, T(\varphi_P) \qquad \text{and} \qquad k_b^{eff} = \varphi_P \rho \frac{k_b\, k_r}{\mu_g}\, T(\varphi_P).$$

For slit pores the partition coefficient can be rephrased as

$$G(\rho) = \frac{H-2d}{H} + \frac{2}{H}\Gamma_{max}\left(\frac{RTZ(\rho)}{\rho RTZ(\rho) + P_L}\right). \tag{2.26}$$

In the computation of the effective parameters $Z(\rho)$ and $\gamma(\rho)$ of the free gas we adopt a Van der Waals equation of state [35]

$$P(\rho) = \rho RTZ(\rho) = RT\frac{\rho}{1-b\rho} - a\rho^2, \tag{2.27}$$

where $a = 27R^2T_c^2/(64P_c)$ and $b = RT_c/(8P_c)$ with P_c and T_c are the critical pressure and temperature respectively.

Under the above representations, the compressibility factor along with the fugacity parameter and Henry's coefficient admit analytical representations [35]

$$Z(\rho) = \frac{1}{1-b\rho} - \rho\frac{a}{RT} \quad , \quad \gamma(\rho) = \frac{\exp\left(Z(\rho) - \rho\frac{a}{RT}\right)}{(1-b\rho)Z(\rho) - 1}, \tag{2.28}$$

$$\mathcal{H}(\rho) = \mathcal{H}^* \exp\left\{v_\infty\left(\frac{\rho RTZ(\rho) - P_{sat}}{RT}\right)\right\}. \tag{2.29}$$

For the computation of the tortuosity function in (2.21)–(2.22), we adopt an isotropic microstructure of spherical interparticle pores. By invoking the self-consistent homogenization scheme we have [3]

$$T(\varphi_P) = \frac{2\varphi_P}{3-\varphi_P}, \tag{2.30}$$

which when inserted in (2.22) gives

$$D^{eff} = \varphi_P\, D_l(S_w)\, \widetilde{g}(P_b)\left(\frac{2\varphi_P}{3-\varphi_P}\right), \tag{2.31}$$

$$k_b^{eff} = \varphi_P\rho\frac{k_b\, k_r}{\mu_g}\left(\frac{2\varphi_P}{3-\varphi_P}\right). \tag{2.32}$$

For the local diffusion coefficient of the gas–water mixture $D_l = D_l(S_w)$ we invoke the experimental relation postulated in Collins et al. [12]

$$D_l(S_w) = D_0 S_w T_w T(\varphi_P) \qquad \text{with} \qquad T_w = S_w^{(2y+1)}. \tag{2.33}$$

Finally, for the relative permeability in (2.20) we adopt Corey's formula

$$k_r = (1-S_{wn})^2(1-S_{wn}^2) \qquad \text{with} \qquad S_{wn} = \frac{S_w - S_{wi}}{1 - S_{wi} - S_{grw}}, \tag{2.34}$$

with S_{wi} and S_{grw} the residual saturation for water and gas respectively.

2.3. **Discretization.** In the sequel, our aim is to illustrate the numerical solution of the forward problem as a motivation for the subsequent optimization procedure by showing the sensitivity of the gas production with different trajectories $\rho_f(t)$. To this end, we discretize the nonlinear parabolic problem (2.23) by the finite element method in conjunction with Newton's algorithm and the backward Euler scheme in time. Thus, begin by introducing the appropriate function spaces. Let $L^2(I)$ be the space of square integrable scalar–valued functions defined in $I = (0,1)$ equipped with the usual inner product

$$(f,g) := \int_0^1 fg\, dy. \tag{2.35}$$

Further let $H^1(I)$ be the subspace of $L^2(I)$ of functions with derivative ∂f in $L^2(I)$ and define $V := \{f \in H^1(I)\,;\, f(0,t) = 0\}$ and $U := \{\rho \in H^1(I)\,;\, \rho(0,t) = \rho_f(t)\}$. Denoting $\{t^n\}$ $(n = 1,2,...,N)$ a partition of the time interval with $\triangle t = t^{n+1} - t^n$, the variational formulation of (2.23) reads as: Find $\rho^{n+1} := \rho(x,t^{n+1}) \in U$ such that

$$\left(R^{n+1}\rho^{n+1}, q\right) + \triangle t\left(K^{\star n+1}\rho_x^{n+1}, q_x\right) = \left(R^n\rho^n, q\right) \qquad \forall q \in V, \tag{2.36}$$

with

$$R^{n+1} := R(\rho^{n+1}) = \varphi_P(1-S_w) + \varphi_P S_w \rho_l RT \frac{Z^{n+1}\gamma^{n+1}}{\mathcal{H}^{n+1}} + \frac{(1-\varphi_P)}{1+\dfrac{\rho_k(1-TOC)(1-\phi_N)}{\rho_I\, TOC}}\phi_N G^{n+1},$$

$$K^{\star n+1} := K^{\star}(\rho^{n+1}) = \varphi_P \left(\rho^{n+1}\frac{k_b\, k_r}{\mu_g} + D_l(S_w)\,\widetilde{g}^{n+1}\right)\left(\frac{2\varphi_P}{3-\varphi_P}\right) \tag{2.37}$$

Denoting $k = 0, 1, ..., K$ the index associated with the iterative Newton–Raphson method we have: Given $\rho^{n+1,k} := \rho^k(x, t^{n+1})$, solution of (2.36) at the k^{th}-iteration, find the subsequent approximation $\rho^{n+1,k+1} := \rho^{k+1}(x, t^{n+1})$ satisfying

$$B\left(\rho^{n+1,k+1}, q\right) = F(\rho^{n+1,k}, q) \qquad \forall q \in V, \tag{2.38}$$

where the bilinear and linear forms are given by

$$\begin{aligned} B(\rho^{n+1,k+1}, w) &= \left(\overline{R}^{n+1,k}\rho^{n+1,k+1}, q\right) + \triangle t\left(K^{\star n+1,k}\rho_x^{n+1,k+1}, q_x\right) + \triangle t\left(\overline{K}^{n+1,k}\rho^{n+1,k+1}, q\right), \\ F(\rho^{n+1,k}, q) &= \left(R'^{n+1,k}(\rho^{n+1,k})^2, q\right) + \triangle t\left(K^{\star\prime n+1,k}\rho^{n+1,k}\rho_x^{n+1,k}\right) + \left(R^n\rho^n, q\right), \end{aligned} \tag{2.39}$$

with

$$\overline{R}^{n+1,k} = R'^{n+1,k}\rho^{n+1,k} + R^{n+1,k} \quad \text{and} \quad \overline{K}^{n+1,k} = K^{\star\prime n+1,k}\frac{\partial}{\partial x}\rho^{n+1,k}. \tag{2.40}$$

By adopting the classical Galerkin approximation, denote $\mathcal{T}_h = \{I^e\}$ a partition of the domain and h the maximum diameter of the elements $I^e \in \mathcal{T}_h$. Further, let $\mathcal{S}_h^k = \{\psi_h \in C^0(I); \psi_h|_{I^e} \in \mathbb{P}_k(I^e)\}$ be the $C^0(\Omega)$ Lagrangian finite element space of degree $k \geq 1$ in each element I^e, with $\mathbb{P}_k(I^e)$ the space of the polynomials of degree $\leq k$ in I^e. The discrete Euler–Galerkin formulation reads as: Given $\rho_h^{n+1,k}$ find $\rho_h^{n+1,k+1} \in U_h \subset U$ such that

$$B\left(\rho_h^{n+1,k+1}, q_h\right) = F(\rho_h^{n+1,k}, q_h) \qquad \forall q_h \in V_h \subset V. \tag{2.41}$$

2.4. **An Illustrative Example.** As quoted before, our aim next is to illustrate the influence of the control variable related to a prescribed pressure (or density $\rho_f(t)$) evolution in time represented by the Dirichlet boundary condition in (2.23) upon gas production. Such preliminary numerical results motivate the development of our subsequent optimization strategy. We then consider three distinct time-decline trajectories of the control variable $\rho_f(t)$. Thus, denote ρ_f^0 and ρ_f^1 the density at the initial and final times related to given pressures P_0 and P_1 at the fracture/well, respectively. The first decay protocol consists of the abrupt scenario, $\rho_f(0) = \rho_f^0$ and $\rho_f(t) = \rho_f^1$ for all time $0 < t < T$ with $\rho_f^1 < \rho_f^0$. In contrast, the second scenario is ruled by a gradual linear decay in the form $\rho_f(t) = (\rho_f^1 - \rho_f^0)t/T + \rho_f^0$ interpolated by piecewise constant functions in some subintervals (t_{i-1}, t_i) for $i \in \{1, 2, 3, ..., n\}$. The last decline consists of a continuum evolution ruled by the same formula, but linearly interpolated in each subinterval. The input coefficients of the forward simulations are displayed in the first column of Table 1.

The three evolutions of the control variable are depicted in Fig. 3 for the same end points $P(\rho_f(0)) = P_0$ and $P(\rho_f(T)) = P_1$. The gas productions is computed by integrating in time the flux at the fracture location $x = 0$. The results presented in Table 2 show the dependence of the gas productions on the decline trajectory. It should be noted that in spite of its enhanced production, the abrupt regime is not feasible in practice due to the possibility of inducing structural damage in the well. To avoid this scenario hereafter we shall pursue alternative pressure/density evolutions with time capable of providing same order of magnitude of the gas production whilst not exhibiting the drawbacks of the abrupt scenario.

3. Optimization Strategy

After constructing and discretizing the forward model governing the hydrodynamics in the shale matrix our aim now is to design the optimal pressure (or density) evolution in time at the production well (or fracture) in order to maximize gas production.

Given a certain a window of time, the main idea underlying the optimization procedure consists in maximizing a family of objective functions where the end–points appear associated with energy and

TABLE 1. Input Data in the Forward Model.

Data	test case	Marcellus	Barnett	Unity
T	36	36	36	month
RT	8.314×378	8.314×378	8.314×355	Pa m^3 / mol
ρ_l	5.556×10^4	5.556×10^4	5.556×10^4	mol / m^3
$\mathcal{H}^*$	5×10^9	5×10^9	5×10^9	Pa
P_{sat}	7×10^5	7×10^5	7×10^5	Pa
v_∞	3.4501×10^{-5}	3.4501×10^{-5}	3.4501×10^{-5}	m^3 / mol
ρ_I	2.7	2.7	2.7	dimensionless
ρ_K	1.2	1.2	1.2	dimensionless
S_w	0.3	0.25	0.3	dimensionless
S_{wi}	0.2	0.2	0.2	dimensionless
S_{grw}	0.2	0.2	0.2	dimensionless
y	0.6527	0.6420	0.6527	dimensionless
D_0	2.4×10^{-9}	2.4×10^{-9}	2.4×10^{-9}	m^2 / s
ϕ_M	0.06	0.06	0.06	dimensionless
ϕ_N	0.1	0.1	0.1	dimensionless
TOC	0.2	0.117	0.05	dimensionless
k_b	10×10^{-19}	5×10^{-19}	1×10^{-19}	m^2
μ_g	2.01×10^{-5}	2.01×10^{-5}	2.01×10^{-5}	Pa s
P_L	4.00×10^6	3.45×10^6	4.48×10^6	Pa
Γ_{max}	$10 \times 10^{18}/\mathrm{nAv}$	$10 \times 10^{18}/\mathrm{nAv}$	$10 \times 10^{18}/\mathrm{nAv}$	mol / m^2
nAv	6.022×10^{23}	6.022×10^{23}	6.022×10^{23}	avogadro's number
H	$3d$	$3d$	$3d$	m
d	0.38×10^{-9}	0.38×10^{-9}	0.38×10^{-9}	m
P_0	24.0×10^6	27.6×10^6	26.2×10^6	Pa
P_1	4.00×10^6	3.45×10^6	6.89×10^6	Pa
T_c	190.6	190.6	190.6	K
P_c	4.599×10^6	4.599×10^6	4.599×10^6	Pa
N_b	70	70	70	number of blocks
H_f	30.0	30.5	30.5	fracture height (m)
W_f	160	198.12	161.7	fracture width (m)
L	9.0	8.7	8.9	block length (m)

TABLE 2. Productions in MMscf ($\times 10^3$) computed in the test case for different declines in the control variable.

	abrupt	gradual	continuum
production	13.47	10.49	10.31

cumulative gas production. The form postulated for the functional reflects the integral in time of the gas flux at the well multiplied by a power law of the density ρ_f. Subsequently within the framework of the adjoint formulation we construct the sensitivity of the objective function with respect to perturbations induced in ρ_f. Information on such a Fréchet derivative provides guidance on the time instant where the well shall be depressurized. Such a methodology illustrates the feasibility of replacing the abrupt regime by a gradual decline leading to smoother production scenarios.

In the sequel, we proceed with the construction of the objective function along with the adjoint problem in order to compute the associated Frechét derivative and optimize production. As quoted before postulate a family of objective functions parametrized by the exponent β with $0 < \beta < 1$ in the form

$$J_\beta(\rho) = -\int_0^T \omega(t)\rho_f(t)^\beta K^\star \rho_x(0,t)dt \,, \tag{3.1}$$

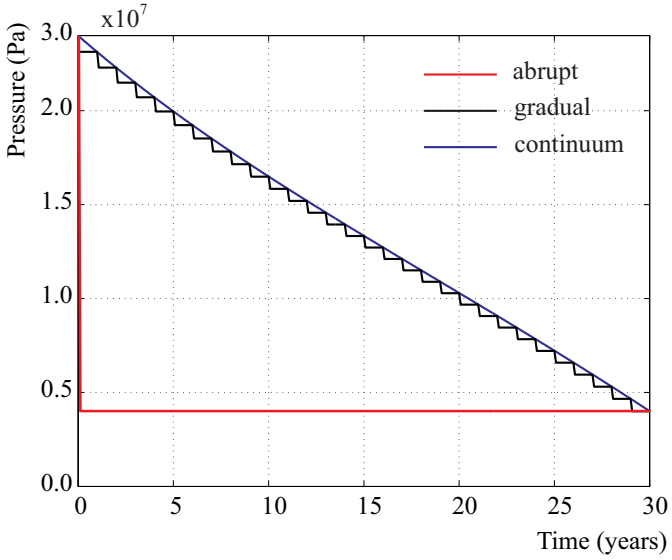

FIGURE 3. Illustration of the heuristic depressurizing protocols.

where $\omega = \omega(t)$ designates a given weight function which strives to incorporate distinct economic scenarios of gas production ruled by the market/energy demand at different periods of time and mainly updates to the present time such as net present values. The minus sign is adopted for convenience in order to pursue the minimum of a cost function. By setting $\omega(t) = 1$, in the asymptotic limits $\beta \to \{0, 1\}$ the objective function degenerates into a cumulative production and the energy stored in the well, respectively.

Throughout the manuscript we shall keep track of the exponent β in order to be capable of recovering the asymptotic limits $\beta \to 0$ and $\beta \to 1$. In order to minimize the cost functional in (3.1), the commonly adopted approaches for computing the sensitivity of $J_\beta(\rho)$ with respect to $\rho_f(t)$ consist of the direct and adjoint methods [7, 8] based on introducing perturbations in the density $\rho_f(t)$ in the form $\rho_f^\varepsilon(t) = \rho_f(t) + \varepsilon\delta\rho_f(t)$ where $\delta\rho_f(0) = 0$ and $\varepsilon > 0$ a small parameter.

3.1. **Direct Approach.** For the sake of completeness, we also present the ideas underlying the direct optimization procedure [7, 8, 22]. To this end, we begin by denoting the upper dot as the Fréchet derivative of a function $\varphi(t)$ with respect to $\rho_f(t)$ in the direction $\delta\rho_f(t)$ defined as

$$\dot{\varphi}(\rho_f) := \lim_{\varepsilon\to 0} \frac{\varphi(\rho_f + \varepsilon\delta\rho_f) - \varphi(\rho_f)}{\varepsilon}, \tag{3.2}$$

and then proceed by computing the derivative of $J(\rho)$ in (3.1) with respect to $\rho_f(t)$

$$\begin{aligned}
\dot{J}(\rho) &= -\int_0^T \omega(t)(\rho_f(t)^\beta(K^\star\dot{\rho}_x + \dot{K}^\star\rho_x)(0,t) + \beta\rho_f(t)^{\beta-1}K^\star\rho_x(0,t)\delta\rho_f(t))\,dt \\
&= -\int_0^T \omega(t)(\rho_f(t)^\beta(K^\star\dot{\rho}_x + (D_\rho K^\star)\dot{\rho}\rho_x)(0,t) + \beta\rho_f(t)^{\beta-1}K^\star\rho_x(0,t)\delta\rho_f(t))\,dt \\
&= -\int_0^T \omega(t)(\rho_f(t)^\beta(K^\star\dot{\rho})_x(0,t) + \beta\rho_f(t)^{\beta-1}K^\star\rho_x(0,t)\delta\rho_f(t))\,dt\,,
\end{aligned} \tag{3.3}$$

with D_ρ denoting the derivative with respect to the gas density. The derivative of the cost functional with respect to $\rho_f(t)$ depends on $\rho(x,t)$ and $\dot{\rho}(x,t)$. Therefore, to compute the derivative of the forward problem with respect to $\rho_f(t)$ we are led to solve the following linear parabolic equation

$$\left\{\begin{array}{rcl}
(\bar{R}\dot{\rho})_t(x,t) - (K^\star\dot{\rho})_{xx}(x,t) &=& 0\,, \quad \text{for} \quad (x,t) \in (0,1)\times(0,T)\,, \\
\dot{\rho}(0,t) &=& \delta\rho_f(t)\,, \\
(K^\star\dot{\rho})_x(1,t) &=& 0\,, \\
\dot{\rho}(x,0) &=& 0\,,
\end{array}\right. \tag{3.4}$$

where $\bar{R} = R + (D_\rho R)\rho$. In order to evaluate the derivative of the cost functional with respect to $\rho_f(t)$, we need to solve (2.23) and (3.4) for each direction $\delta\rho_f(t)$. In spite of its simplicity, such a procedure is impracticable due to the high computational cost involved.

3.2. **Adjoint Approach.** Within the present alternative methodology for computing $\dot{J}(\rho)$ we proceed within the adjoint-based approach [7, 8, 22], where the derivative (3.3) is decomposed in the form $\dot{J}(\rho) = \langle D_\rho J, \dot{\rho}\rangle + \langle \partial_{\rho_f} J, \delta\rho_f\rangle$, with

$$\begin{aligned} \langle D_\rho J, \dot{\rho}\rangle &= -\int_0^T \omega(t)\rho_f(t)^\beta (K^\star\dot{\rho})_x(0,t)\ dt\ , \\ \langle \partial_{\rho_f} J, \delta\rho_f\rangle &= -\int_0^T \beta\omega(t)\rho_f(t)^{\beta-1} K^\star\rho_x(0,t)\delta\rho_f(t)\ dt\ . \end{aligned} \tag{3.5}$$

The term involving $\langle D_\rho J, \dot{\rho}\rangle$ can be rewritten as follows

$$\begin{aligned} \langle D_\rho J, \dot{\rho}\rangle &= \int_0^T\int_0^1 \omega(t)\rho_f(t)^{\beta-1}(\rho(K^\star\dot{\rho})_x)_x(x,t)\ dxdt \\ &= \int_0^T\int_0^1 \omega(t)\rho_f(t)^{\beta-1}(\rho_x(K^\star\dot{\rho})_x + \rho(K^\star\dot{\rho})_{xx})(x,t)\ dxdt\ . \end{aligned} \tag{3.6}$$

In which, after integration by parts gives for the last term

$$\begin{aligned} \int_0^1 \omega(t)\rho_f(t)^{\beta-1}\rho(K^\star\dot{\rho})_{xx}(x,t)\ dx = &-\int_0^1 \omega(t)\rho_f(t)^{\beta-1}\rho_x(K^\star\dot{\rho})_x(x,t)\ dx + \\ &+\omega(t)\rho_f(t)^{\beta-1}(\rho(K^\star\dot{\rho})_x(1,t) - \rho(K^\star\dot{\rho})_x(0,t))\ . \end{aligned} \tag{3.7}$$

Hence, using the boundary conditions (2.23) we have for the first term

$$\begin{aligned} \int_0^1 \omega(t)\rho_f(t)^{\beta-1}\rho(K^\star\dot{\rho})_{xx}(x,t)\ dx = &-\int_0^1 \omega(t)\rho_f(t)^{\beta-1}\rho_x(K^\star\dot{\rho})_x(x,t)\ dx \\ &-\omega(t)\rho_f(t)^\beta(K^\star\dot{\rho})_x(0,t). \end{aligned} \tag{3.8}$$

Therefore, using the governing equation (3.4) we have from (3.6)

$$\langle D_\rho J, \dot{\rho}\rangle = \int_0^T\int_0^1 \omega(t)\rho_f(t)^{\beta-1}(\rho_x(K^\star\dot{\rho})_x + (\bar{R}\dot{\rho})_t\rho)(x,t)\ dxdt\ . \tag{3.9}$$

Hence, integrating by parts gives

$$\begin{aligned} \langle D_\rho J, \dot{\rho}\rangle = &\int_0^T\int_0^1 \omega(t)\rho_f(t)^{\beta-1}\rho_x(K^\star\dot{\rho})_x(x,t)\ dxdt - \\ &-\int_0^T\int_0^1 [\omega(t)\rho_f(t)^{\beta-1}\rho(x,t)]_t\bar{R}\dot{\rho}(x,t)\ dxdt + \\ &+\int_0^1 \omega(T)\rho_f(T)^{\beta-1}\bar{R}\dot{\rho}\rho(x,T)\ dx\ , \end{aligned} \tag{3.10}$$

where we have used the initial condition in (3.4). We now proceed by introducing the adjoint state in the form $V = V(x,t) := \omega(t)\rho_f(t)^{\beta-1}\rho(0,t) - \lambda(x,t)$, where λ is the solution of the following linear parabolic equation

$$\left\{\begin{array}{rcl} \bar{R}\lambda_t(x,t) + K^\star\lambda_{xx}(x,t) &=& 0\ , \quad \text{for} \quad (x,t)\in(0,1)\times(0,T)\ , \\ \lambda(0,t) &=& \omega(t)\rho_f(t)^\beta\ , \\ K^\star\lambda_x(1,t) &=& 0\ , \\ \lambda(x,T) &=& 0\ , \end{array}\right. \tag{3.11}$$

Note that $V(x,t)$ satisfies a time reverse problem with a prescribed final condition. Adopting the change of variable $\tau = T - t$, we have $V_\tau = -V_t$ and thus $\lambda_\tau = -\lambda_t$. Consequently the adjoint problem (3.11)

can be rewritten in the usual evolutionary form

$$\left\{\begin{array}{rcl} \bar{R}\lambda_\tau(x,\tau) - K^\star\lambda_{xx}(x,\tau) &=& 0\ , \quad \text{for} \quad (x,\tau)\in(0,1)\times(0,T)\ , \\ \lambda(0,\tau) &=& \omega(t)\rho_f(t)^\beta\ , \\ K^\star\lambda_x(1,\tau) &=& 0\ , \\ \lambda(x,0) &=& 0\ . \end{array}\right. \tag{3.12}$$

In the sequel, we present the variational statement associated with (3.4) and (3.12). To this end, introduce the set $\mathcal{U}$ and the space $\mathcal{V}$ in the form

$$\mathcal{U} = \{\varphi\in H^1(0,1) : \varphi_{|_{x=0}} = \delta\rho_f\} \quad \text{and} \quad \mathcal{V} = \{\varphi\in H^1(0,1) : \varphi_{|_{x=0}} = 0\}\ . \tag{3.13}$$

The weak form of (3.4) consists in: Given the homogeneous initial condition, for each $t\in(0,T)$, find $\dot\rho\in\mathcal{U}$, such that

$$\int_0^1 (\bar{R}\dot\rho)_t\Phi\ dx + \int_0^1 (K^\star\dot\rho)_x\Phi_x\ dx = 0 \quad \forall\Phi\in\mathcal{V}\ . \tag{3.14}$$

In addition, the weak form associated with the adjoint problem (3.12) reads as: Given the final condition $\rho(x,T)$, for each $t\in(0,T)$, find $V\in\mathcal{V}$, such that

$$\int_0^1 \bar{R}V_t\Phi\ dx - \int_0^1 V_x(K^\star\Phi)_x\ dx = \int_0^1 \bar{R}(\omega\rho_f^{\beta-1}\rho)_t\Phi - \int_0^1 \omega\rho_f^{\beta-1}\rho_x(K^\star\Phi)_x\ dx \quad \forall\Phi\in\mathcal{V}\ . \tag{3.15}$$

Since $V\in\mathcal{V}$, we may choose $\Psi = V$ in (3.14) to obtain

$$\int_0^1 (\bar{R}\dot\rho)_t V\ dx + \int_0^1 (K^\star\dot\rho)_x V_x\ dx = 0\ . \tag{3.16}$$

Hence, integrating by parts and using the initial and final conditions in (3.4) and (3.11), respectively gives

$$\int_0^T\int_0^1 (\bar{R}\dot\rho V_t - (K^\star\dot\rho)_x V_x)\ dxdt = \int_0^1 \omega(T)\rho_f(T)^{\beta-1}\bar{R}\dot\rho\rho(x,T)\ dx\ . \tag{3.17}$$

Now, choose $\Phi = \dot\rho - \Psi$ as a test function in (3.15), where Ψ is the lifting of the Dirichlet boundary data $\delta\rho_f$, namely, $\Psi(0,t) = \delta\rho_f(t)$. This yields

$$\begin{aligned} \int_0^1 \bar{R}V_t(\dot\rho-\Psi)\ dx - \int_0^1 V_x(K^\star(\dot\rho-\Psi))_x\ dx = \\ = \int_0^1 \bar{R}(\omega\rho_f^{\beta-1}\rho)_t(\dot\rho-\Psi) - \int_0^1 \omega\rho_f^{\beta-1}\rho_x(K^\star(\dot\rho-\Psi))_x\ dx\ . \end{aligned} \tag{3.18}$$

Hence, after some manipulations we obtain

$$\begin{aligned} \int_0^1 \bar{R}(\omega\rho_f^{\beta-1}\rho)_t\dot\rho\ dx - \int_0^1 \omega\rho_f^{\beta-1}\rho_x(K^\star\dot\rho)_x\ dx = \\ = \int_0^1 \bar{R}\dot\rho V_t\ dx - \int_0^1 (K^\star\dot\rho)_x V_x\ dx + \int_0^1 \bar{R}(\omega\rho_f^{\beta-1}\rho)_t\Psi - \\ - \int_0^1 \omega\rho_f^{\beta-1}\rho_x(K^\star\Psi)_x\ dx - \int_0^1 \bar{R}V_t\Psi\ dx + \int_0^1 V_x(K^\star\Psi)_x\ dx\ . \end{aligned} \tag{3.19}$$

Integrating by parts furnishes

$$\begin{aligned} \int_0^1 \omega\rho_f^{\beta-1}\rho_x(K^\star\Psi)_x\ dx &=& \omega\rho_f^{\beta-1}(K^\star\rho_x\Psi(1,t) - K^\star\rho_x\Psi(0,t)) - \int_0^1 \omega\rho_f^{\beta-1}K^\star\rho_{xx}\Psi\ dx \\ &=& -\omega\rho_f^{\beta-1}K^\star\rho_x(0,t)\delta\rho_f(t) - \int_0^1 \omega\rho_f^{\beta-1}K^\star\rho_{xx}\Psi\ dx\ , \end{aligned} \tag{3.20}$$

where the boundary conditions $K^\star\rho_x(1,t) = 0$ and $\Psi(0,t) = \delta\rho_f(t)$ have been used. In a similar fashion, we have

$$\begin{aligned}\int_0^1 V_x(K^\star\Psi)_x\,dx &= K^\star V_x(1,t)\Psi(1,t) - K^\star V_x(0,t)\Psi(0,t) - \int_0^1 (K^\star V_x)_x\Psi\,dx \\ &= -K^\star V_x(0,t)\delta\rho_f(t) - \int_0^1 (K^\star V_x)_x\Psi\,dx\,. \end{aligned} \tag{3.21}$$

Since $K^\star V_x(1,t) = 0$ and again using the boundary condition for $\Psi(0,t)$ we have

$$\begin{aligned}&\int_0^1 \bar{R}(\omega\rho_f^{\beta-1}\rho)_t\dot{\rho}\,dx - \int_0^1 \omega\rho_f^{\beta-1}\rho_x(K^\star\dot{\rho})_x\,dx = \\ &\quad= \int_0^1 \bar{R}\dot{\rho}V_t\,dx - \int_0^1 (K^\star\dot{\rho})_x V_x\,dx + \omega\rho_f^{\beta-1}K^\star\rho_x(0,t)\delta\rho_f(t) - K^\star V_x(0,t)\delta\rho_f(t) - \\ &\qquad - \int_0^1 (\bar{R}(V_t - (\omega\rho_f^{\beta-1}\rho)_t) + K^\star V_{xx} - \omega\rho_f^{\beta-1}K^\star\rho_{xx})\Psi\,dx\,. \end{aligned} \tag{3.22}$$

Since $V(x,t)$ satisfies the adjoint problem (3.11) the last term vanishes. Hence, integration in time leads to

$$\begin{aligned}\int_0^T\int_0^1 (\bar{R}(\omega\rho_f^{\beta-1}\rho)_t\dot{\rho} - \omega\rho_f^{\beta-1}\rho_x(K^\star\dot{\rho})_x)\,dxdt &= \int_0^T\int_0^1 (\bar{R}\dot{\rho}V_t - (K^\star\dot{\rho})_x V_x)\,dxdt \\ &+ \int_0^T \omega\rho_f^{\beta-1}K^\star\rho_x(0,t)\delta\rho_f(t)\,dt - \int_0^T K^\star V_x(0,t)\delta\rho_f(t)\,dt\,. \end{aligned} \tag{3.23}$$

in which when combined with (3.17) gives

$$\begin{aligned}\int_0^T\int_0^1 (\bar{R}(\omega\rho_f^{\beta-1}\rho)_t\dot{\rho} - \omega\rho_f^{\beta-1}\rho_x(K^\star\dot{\rho})_x)\,dxdt &= \int_0^1 \omega(T)\rho_f(T)^{\beta-1}\bar{R}\dot{\rho}\rho(x,T)\,dx \\ &+ \int_0^T \omega\rho_f^{\beta-1}K^\star\rho_x(0,t)\delta\rho_f(t)\,dt - \int_0^T K^\star V_x(0,t)\delta\rho_f(t)\,dt\,. \end{aligned} \tag{3.24}$$

Finally, the derivative $\langle D_\rho J, \dot{\rho}\rangle$ in (2.23) and (2.27) can be represented in the form

$$\langle D_\rho J, \dot{\rho}\rangle = -\int_0^T \omega\rho_f(t)^{\beta-1}K^\star\rho_x(0,t)\delta\rho_f(t)\,dt + \int_0^T K^\star V_x(0,t)\delta\rho_f(t)\,dt\,. \tag{3.25}$$

From the above results, the Fréchet derivative of the cost functional $J(\rho)$ with respect to $\rho_f(t)$ in the direction $\delta\rho_f(t)$ can be represented in the form

$$\dot{J}(\rho) = -\int_0^T (1+\beta)\omega(t)\rho_f(t)^{\beta-1}K^\star\rho_x(0,t)\delta\rho_f(t)\,dt + \int_0^T K^\star V_x(0,t)\delta\rho_f(t)\,dt \quad \forall\delta\rho_f(t)\,. \tag{3.26}$$

Since the perturbation $\delta\rho_f(t)$ is arbitrary, we can identify the derivative $D_{\rho_f}J(\rho)$ in the form

$$D_{\rho_f}J(\rho)(t) = -(1+\beta)\omega(t)\rho_f(t)^{\beta-1}K^\star\rho_x(0,t) + K^\star V_x(0,t)\,. \tag{3.27}$$

where the gas density $\rho(x,t)$ is solution to the forward non-linear system (2.23) and $V(x,t)$ satisfying the adjoint linear system (3.11), or equivalently solution of the time reverse parabolic problem (3.12).

Remark 1. *The above representation of the derivative can also be derived within the framework of the augmented Lagrangian formalism by envisioning the problem in terms of minimizing the cost function* (3.1) *subject to the state equation* (2.23)*. Such a constrained optimization statement can be rewritten in the form of an unconstrained problem by introducing the Lagrangian functional*

$$L_\beta(\rho,\lambda) = -\int_0^T \omega(t)\rho_f(t)^\beta K^\star\rho_x(0,t)\,dt + \int_0^T\int_0^1 [(R\rho)_t(x,t) - (K^\star\rho_x)_x(x,t)]\lambda(x,t)\,dx\,dt\,. \tag{3.28}$$

Since ρ_f, ρ and λ are assumed to be independent, the total variation of the augmented Lagrangian functional $L_\beta(\rho,\lambda)$ with respect to the control variable ρ_f is given by the sum

$$\dot{L}_\beta(\rho,\lambda) = \langle D_{\rho_f} L_\beta(\rho,\lambda), \delta\rho_f\rangle + \langle D_\rho L_\beta(\rho,\lambda), \delta\rho\rangle + \langle D_\lambda L_\beta(\rho,\lambda), \delta\lambda\rangle \ . \tag{3.29}$$

The variations $\langle D_\rho L_\beta(\rho,\lambda), \delta\rho\rangle$ and $\langle D_\lambda L_\beta(\rho,\lambda), \delta\lambda\rangle$ vanish provided that ρ and λ are solutions of (2.23) *and* (3.11)*, respectively. Therefore, we have*

$$\dot{L}_\beta(\rho,\lambda) = \langle D_{\rho_f} L_\beta(\rho,\lambda), \delta\rho_f\rangle = -\int_0^T K^\star(\beta\omega(t)\rho_f(t)^{\beta-1}\rho_x(0,t) + \lambda_x(0,t))\delta\rho_f(t)\, dt \ , \tag{3.30}$$

which corroborates with (3.26) *since $\lambda(x,t) = \omega(t)\rho_f(t)^{\beta-1}\rho(0,t) - V(x,t)$.*

3.3. **Optimization Algorithm.** The aforementioned representation for the Fréchet derivative allows to develop an optimization strategy to pursue the minimum of the cost function. In the sequel, we present the numerical algorithm for constructing the optimal trajectory $\rho_f = \rho_f(t)$ that minimizes $J(\rho)$. We shall explore (3.27) as an indicator of the steepest-descent direction of the objective function (3.1). Thus, set the descent direction as

$$\delta\rho_f(t) = -D_{\rho_f} J(\rho)(t). \tag{3.31}$$

By proceeding in an iterative fashion, the resulting algorithm can be summarized as follows: Denoting n as an integer positive associated with the iterative loop, set

$$\rho_f^{n+1}(t) = \rho_f^n(t) - \kappa\, D_{\rho_f} J(\rho^n)(t), \tag{3.32}$$

and enforce monotonicity

$$\rho_f^{n+1}(t) \geq \rho_f^{n+1}(t+\delta t), \text{ with } \delta t > 0, \tag{3.33}$$

where κ denotes the step size determined by a line-search algorithm performed to ensure a decreasing of the objective functional $J(\rho)$, namely

$$\kappa : J(\rho^{n+1}) < J(\rho^n). \tag{3.34}$$

We then construct the following optimization algorithm:

(1) In each iteration n solve the forward problem (2.23) for ρ^n.
(2) Solve the adjoint problem (3.12) for V^n.
(3) Compute the derivative (3.27) of the objective function.
(4) Begin by setting $\kappa = 1$, and update the density profile according to (3.32)–(3.33).
(5) Given a small tolerance κ^* compute the cost function from (3.1)
   - if $J(\rho^{n+1}) < J(\rho^n)$, evolve in the iterative process;
   - if $J(\rho^{n+1}) > J(\rho^n)$, set $\kappa \leftarrow \kappa/2$ while $\kappa > \kappa^*$;
   - if $\kappa \leq \kappa^*$, stop.

4. Numerical Results

After constructing the proper algorithm for computing the minimum of the cost function for a prescribed weight function $\omega(t)$ and exponent β, we are now ready to illustrate the performance of the proposed methodology. To this end, our subsequent numerical simulations are performed in the same experiment of section 2.4 with input data extracted from Marcellus and Barnett formation (Table 1 2nd and 3th columns). The first set of simulations does not incorporate the influence of the weight function ($\omega(t) = 1$). In Figs. 4 and 5 we begin by displaying the evolution of the normalized derivatives of the objective functional $d_{\rho_f}(t) := D_{\rho_f} J(\rho)(t)/\ \|D_{\rho_f} J(\rho)(t)\|$at the first and last iterations for $\beta = 0$ and $\beta = 1$ respectively. In both cases the derivative in the first iteration $n = 0$ suggests a fast depressurization initially whereas in the last iteration, we observe the appearance of peaks at the end of the time interval due to the enforcement of the physical constraint $P(\rho_f(t)) \geq P_1$, which has to be fulfilled for all time t.

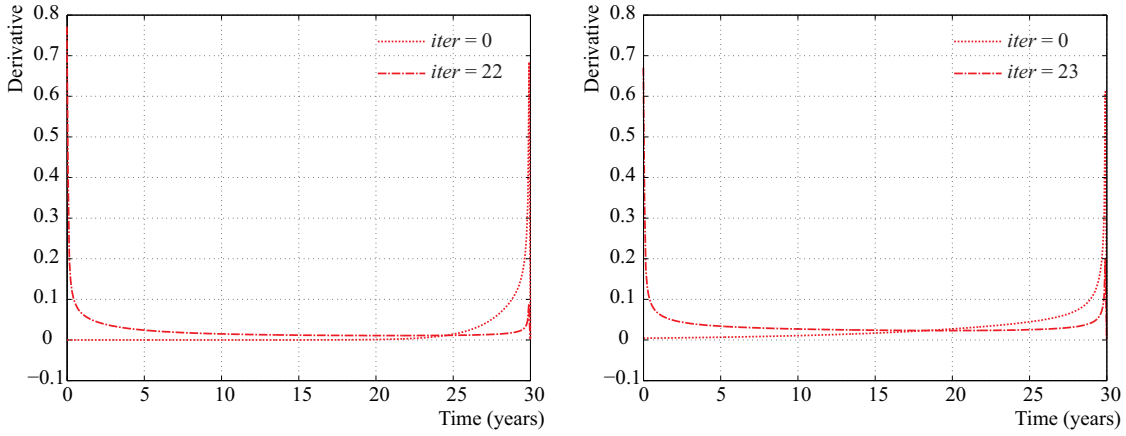

(a) Marcellus (b) Barnett

FIGURE 4. Normalized derivatives of the objective function $d_{\rho_f}(t)$ at the first (dashed line) and last (dashed dotted line) iterations for $\beta = 0$.

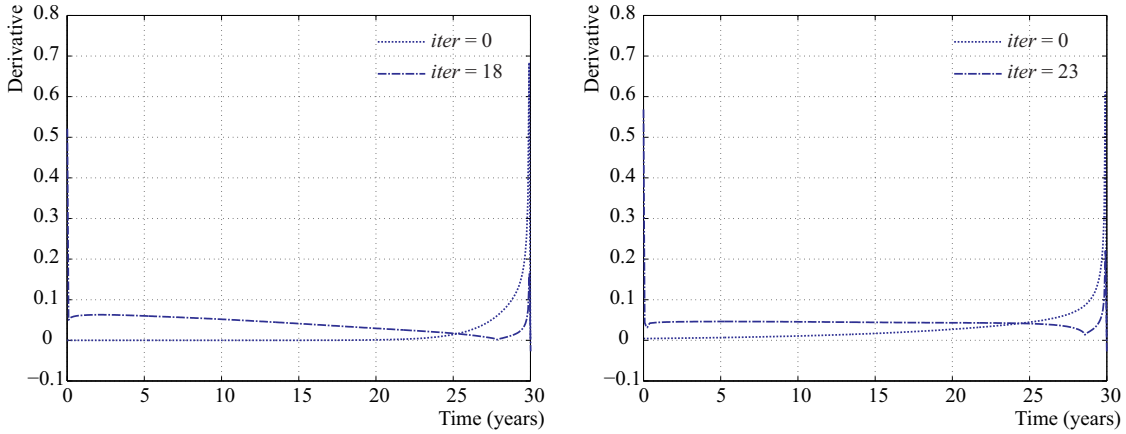

(a) Marcellus (b) Barnett

FIGURE 5. Normalized derivatives of the objective function $d_{\rho_f}(t)$ at the first (dashed line) and last (dashed dotted line) iterations for $\beta = 1$.

The associated decline trajectories of the control variable $\rho_f(t)$ are depicted in Fig. 6 for the two geological formations. Recalling that for $\beta = 0$ and $\omega(t) = 1$ the objective function degenerates into the cumulative production at the well. In this case the algorithm converges to the abrupt depletion of ρ_f as expected. On the other hand, for $\beta = 1$, the product between flux and density characterizes $J(\rho)$ as an energy-based quantity whose minimization furnishes an alternative smoother controlled density dissipation. It is worth noting that for $\beta = 1$ the scenario associated with the Marcellus formation of higher permeability suggests a nearly linear decline whereas in the case of the more impermeable Barnett a nonlinear decline is suggested more pronounced for large time.

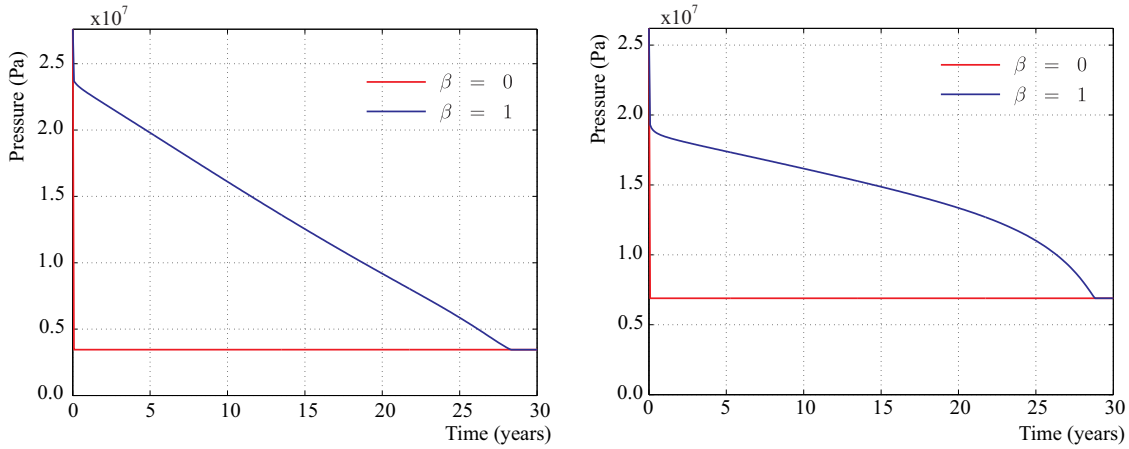

(a) Marcellus (b) Barnett

FIGURE 6. Computed decline trajectories in the controlled density for $\beta = 0$ and $\beta = 1$.

The spatial density profiles associated with the forward and adjoint problems parametrized by time are plotted in Fig. 7 in the case $\beta = 1$.

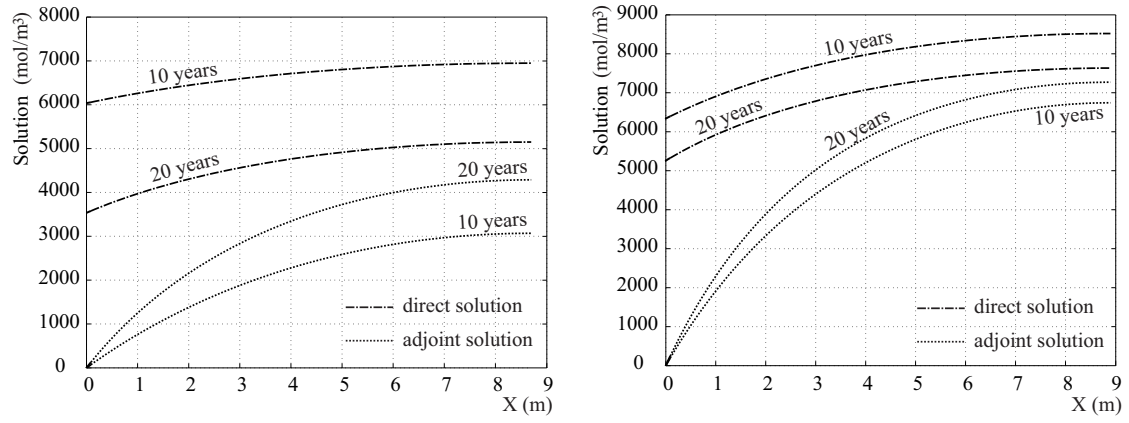

(a) Marcellus (b) Barnett

FIGURE 7. Density profiles for the forward and adjoint problems for $\beta = 1$.

As expected the decline in the controlled density $\rho_f(t)$ at $x = 0$ leads to a gradual decrease in the $\rho(x,t)$ with time. Conversely the time-reversal nature of the adjoint state leads to an increase in the magnitude of $V(x,t)$ constrained by the enforcement of the homogeneous Dirichlet condition at $x = 0$. In Fig. 8 we display the evolution in time of the gas flux at the well. It should be noted that the abrupt case ($\beta = 0$) is characterized by a large peak at $t = 0$, whereas in the smoother case ($\beta = 1$) two small peaks appear at $t = 0$ and $t \approx 27$ years. The related cumulative productions are displayed in Fig. 9. As expected higher values are obtained for $\beta = 0$ where the functional degenerates into cumulative production

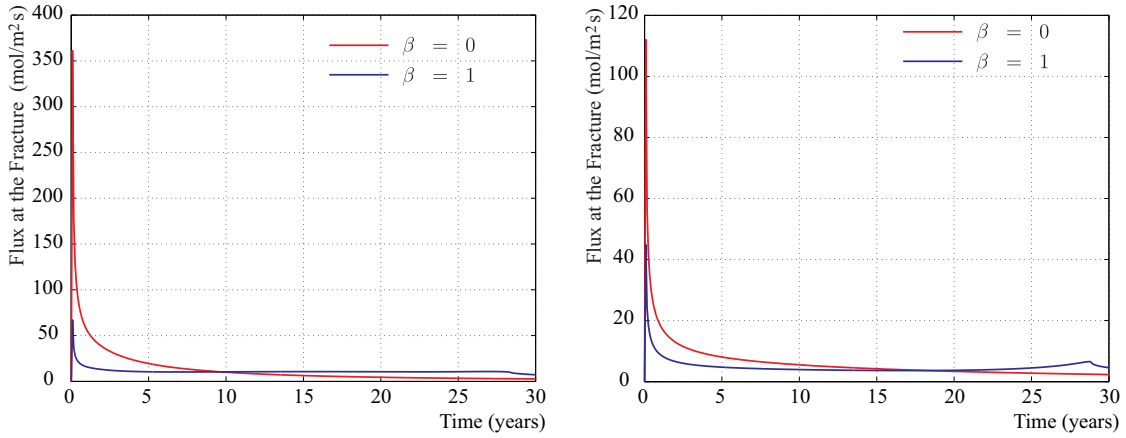

(a) Marcellus (b) Barnett

FIGURE 8. Evolution of the gas flux at the well $K^\star(0,t)\rho_x(0,t)$ for $\beta = 0$ and $\beta = 1$.

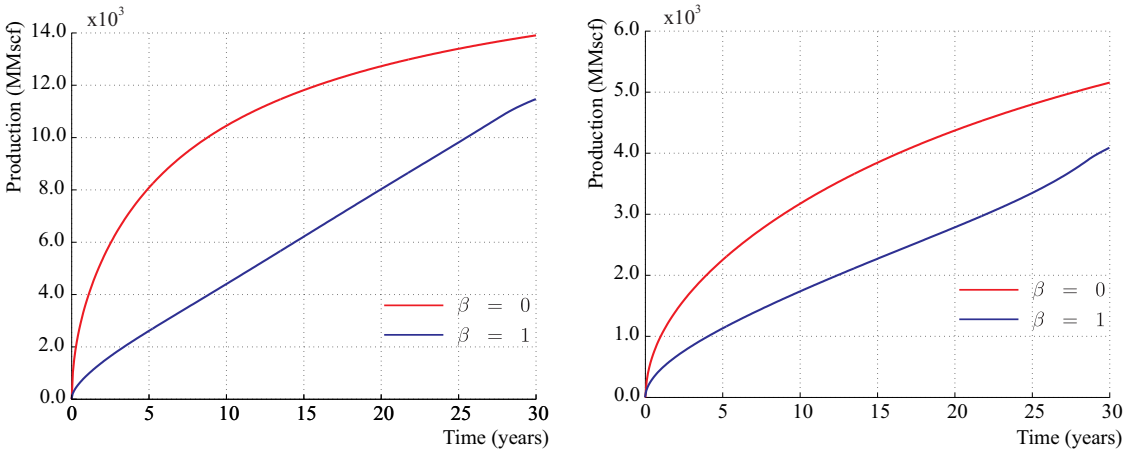

(a) Marcellus (b) Barnett

FIGURE 9. Obtained cumulative production for $\beta = 0$ in red and $\beta = 1$ in blue.

TABLE 3. Cumulative production in MMscf ($\times 10^3$) computed with the optimized scenarios for the Marcellus and Barnett fields.

	$\beta = 0$	$\beta = 1$
Marcellus	13.91	11.46
Barnett	5.16	4.08

The evolution of the objective function $J(\rho^n)$ in the iterative process is shown in Fig. 10 for Marcellus and Barnett formations. We may verify monotonic decay with the number of interactions tending asymptotically to a minimum. Such a nice property illustrates the potential of the optimization procedure proposed herein. Since the values of the derivatives $D_{\rho f} J(\rho)(t)$ in the last iterations for both $\beta = 0$ and $\beta = 1$ are uniform and very small, the evolution process overcomes possible stagnation points with limit tending to a local (or global) minimum.

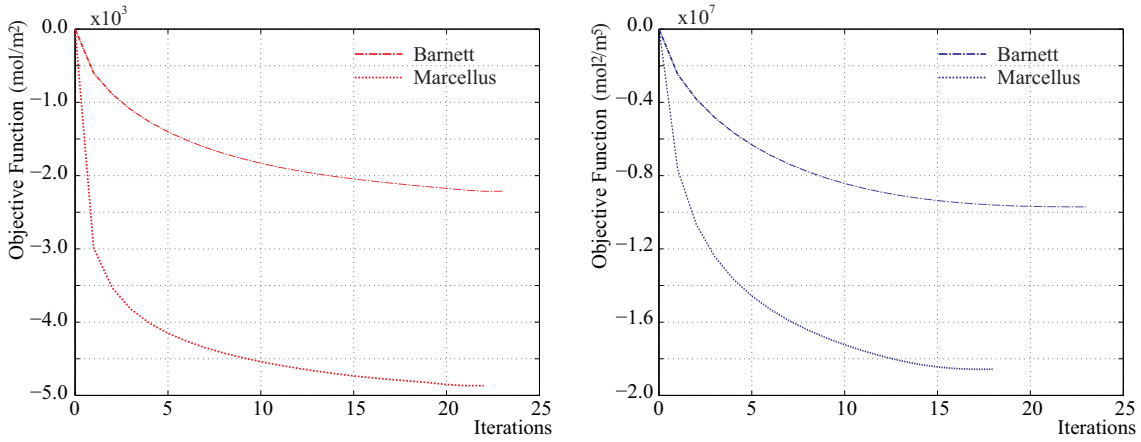

(a) $\beta = 0$ (b) $\beta = 1$

FIGURE 10. Evolution of the objective function $J(\rho^n)$ with the number of iterations.

Our final set of simulations aims at illustrating the influence of the weight function $\omega(t)$ on gas production in order to comply with high and low demanding scenarios and also updates to the present value (NPV) [47]. Thus, we restrict our subsequent analysis to the case $\beta = 0 (J_\beta = J_0)$ where the objective function degenerates into cumulative production weighted by $\omega(t)$ which will suitably chosen in order to the functional represent the net present value (NPV) [47]. We then have

$$J_0(\rho) = -\int_0^T \omega(t) K^\star \rho_x(0,t) dt \ . \tag{4.1}$$

Thus, in the current context the NPV–function is defined in the form [47]

$$\text{NPV} = \int_0^T \frac{C(t)}{\exp(rt)} \ , \tag{4.2}$$

where $C(t)$ designates the net cash flow and r the appropriate discount rate, which is set as $r = 0.1$ per year. In order to comply with (4.1) consider the decomposition

$$C(t) := \alpha(t) K^\star \rho_x(0,t) \ , \tag{4.3}$$

so that the weight function $\omega(t)$ can be identified as

$$\omega(t) = \frac{\alpha(t)}{\exp(rt)} \ . \tag{4.4}$$

In our subsequent numerical simulation, we consider three different scenarios for $\alpha(t)$ whose prescribed time–evolution incorporates market change scenarios not including production and interest rate. Thus, we have

$$\alpha_1(t) := 8\,\frac{t-3}{T}, \quad \alpha_2(t) := 16\,\sin^2\left(\frac{3\pi t}{2T}\right)\left(\frac{t}{T}\right)^2 \quad \text{and} \quad \alpha_3(t) := 2\,\frac{\log(t+1)}{\log(T+1)} \ . \tag{4.5}$$

with associated weight functions displayed in Fig. 11.

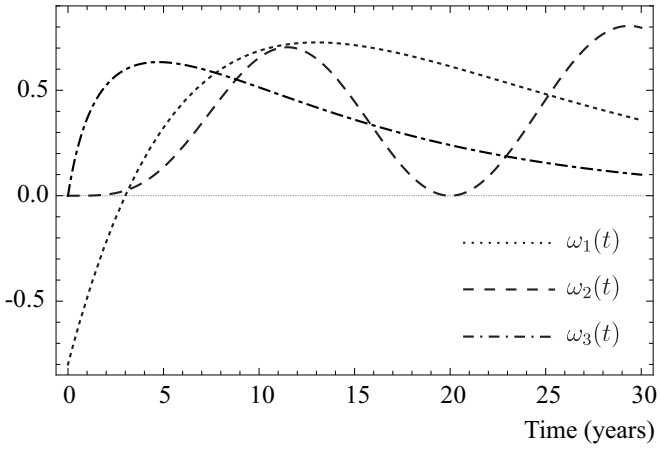

FIGURE 11. Representation of the three different weight functions.

We remark that non–monotone behavior was postulated for $\alpha(t)$ in order to accommodate additional production costs during the period possibly related to the necessity of re–fracking. In particular, initially the function $\alpha_1(t)$ admits negative values owing to the necessity of prior investment.

The resulting optimal trajectories $\rho_f(t)$ are shown in Fig. 12. It is remarkable to see completely different declines compared to the previous cases of unitary weight function. In particular for $\omega_1(t)$ and $\omega_2(t)$, we may observe the avoidance of producting at earlier times where $\omega_1(t)$ is negative and $\omega_2(t)$ grows slowly. On the other hand, after 5 years both weight functions grow faster inducing a more pronounced declining. We also observe a large plateau in the well pressure between 10 and 25 years, since $\omega_2(t)$ exhibits a valley around 20 years (Fig. 11). In addition, since $\omega_3(t)$ grows rapidly at the beginning of the time interval, large dissipation in the well pressure is required initially. Finally, we may observe that all cases suggest avoidance of the abrupt scenario showing the striking feature of the optimization strategy in the case of time–dependent weight functions with the objective function represented by the NPV. Adopting the choice $r = 0.1$ and 4500 dollars per MMscf of gas, the resulting profits are presented in Fig. 13. We may observe substantial improvement in the profit for the optimized solutions thus illustrating the remarkable achievement of the proposed strategy.

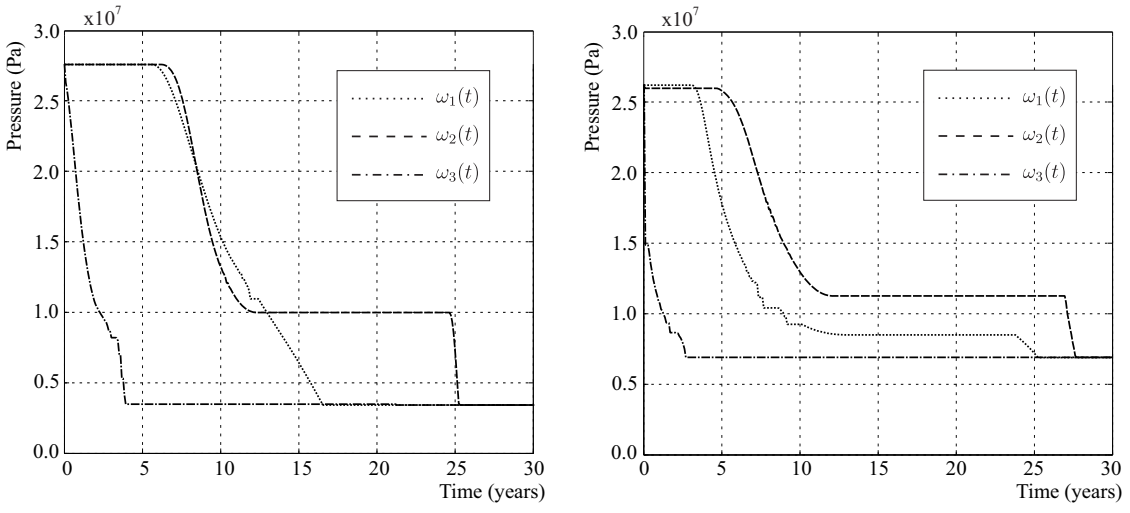

(a) Marcellus (b) Barnett

FIGURE 12. Optimal declining trajectories for time–dependent weight functions.

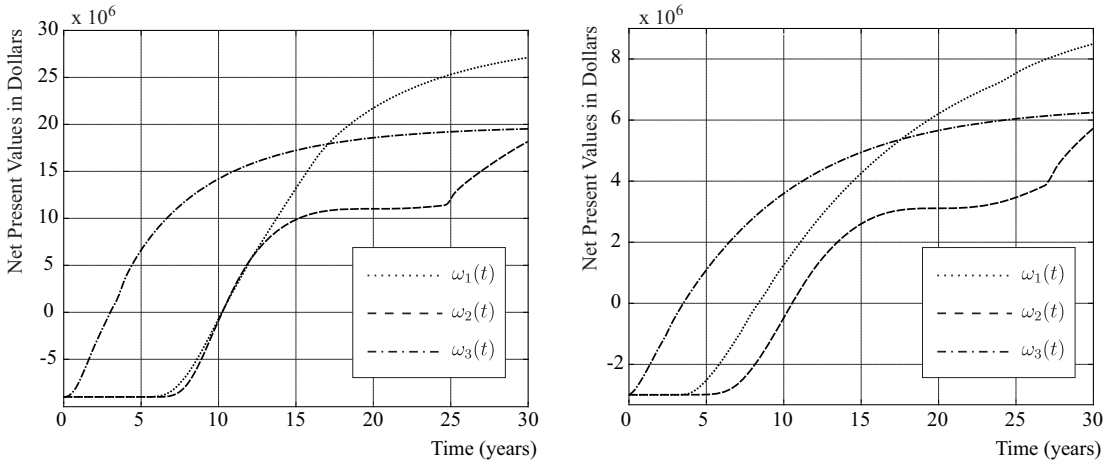

(a) Marcellus (b) Barnett

FIGURE 13. Cumulative profit computed with the chosen weight functions.

The NPV are presented in Tables 4, 5 and 6 for the three weight functions. It should be noted that overall productions are smaller than the ones obtained in the abrupt scenario for $\beta = 0$ and $\omega(t) = 1$ (see Table 3, first column). Conversely, by choosing a NPV–based functional gives rise to higher profits adopting the optimized decline trajectories. It is worth noting that, since $\omega_1(t)$ is negative for $t < 3$ years, the abrupt protocol leads to loss rather than profit, while the optimized trajectory produces the highest profit. Finally, since $\omega_3(t)$ grows faster at earlier times, the resulting profits for both optimized and *ad hoc* protocols are of same order of magnitude with a slight improvement observed for the optimized decline.

TABLE 4. Cumulative productions in MMscf ($\times 10^3$) computed with time–dependent weight functions for the Marcellus and Barnett formations.

	ω_1	ω_2	ω_3
Marcellus	12.49	11.38	13.66
Barnett	4.65	4.13	5.13

TABLE 5. Net Present Values in Dollars ($\times 10^6$) computed with time–dependent weight functions for the Marcellus formation.

	ω_1	ω_2	ω_3
Abrupt *(ad hoc)*	-6.84	2.32	15.48
Optimized	27.11	18.16	19.54

TABLE 6. Net Present Values in Dollars ($\times 10^6$) computed with time–dependent weight functions for the Barnett formation.

	ω_1	ω_2	ω_3
Abrupt *(ad hoc)*	1.27	2.56	5.91
Optimized	8.49	5.72	6.25

5. Remarks on Geomechanical Effects

For the sake of simplicity the forward–optimization models developed herein were presented for gas flow in a rigid medium. In order to develop the proper extension to incorporate poroelastic effects in the shale matrix, we can explore the constitutive law postulated by Coussy for the fluid content and Lagragian porosity ϕ combined with the effective stress principles for the total stress. In the sequel, we present the first steps toward this extension. Following Coussy [13], for deformable media the overall porosity including micro and nanoporosity contributions is treated as a transient Lagrangian quantity which for a linear poroelatic skeleton admits the constitutive law

$$\phi(t) = \phi^0 + \alpha \nabla \cdot \boldsymbol{u} + \frac{1}{N}(P_b - P_b^0), \tag{5.1}$$

where the superscript "0"denotes the reference state, $\boldsymbol{u}$ the displacement of the rock, α the Biot–Wills parameters and N^{-1} the undrained compressibility solely associated with the solid grains given by

$$\alpha = 1 - \frac{K}{K_s} \qquad \text{and} \qquad \frac{1}{N} = \frac{\alpha - \phi^0}{K_s}, \tag{5.2}$$

with K and K_s the bulk modulus of the matrix and grains respectively. Given the fractions of organic and inorganic matters and porosities, the dependence the poroelastic parameters on (TOC, ϕ_n, φ_P) can be computed by invoking the self–consistent approach [3]. Thus, assuming that the time evolution of $\phi(t)$ due to geomechanical effects is mainly dictated by $\varphi_P(t)$ we have

$$\frac{\partial}{\partial t}\left(R^g(P_b)\, P_b\right) + \nabla \cdot \boldsymbol{J}_b = 0 \qquad \text{in} \quad \Omega_s \times (0,T), \tag{5.3}$$

with R^g given in (2.18) with transient $\varphi_P(t) \approx \phi(t)$ governed by (5.1). The above result together with (2.18) and (5.1) govern the hydrodynamics.

The aforementioned mass balance can be combined with the classical Biot formulation of the effective stress principle given by

$$\begin{array}{rcl} \nabla \cdot \boldsymbol{\sigma_T} & = & 0 \\ \boldsymbol{\sigma_T} & = & \boldsymbol{\sigma_E} - \alpha P_b \boldsymbol{I}\ , \\ \boldsymbol{\sigma_E} & = & \boldsymbol{C}\mathcal{E}(\boldsymbol{u})\ , \\ \mathcal{E}(\boldsymbol{u}) & = & \dfrac{1}{2}\left(\nabla \boldsymbol{u} + \nabla^t \boldsymbol{u}\right)\ , \end{array} \tag{5.4}$$

where $\boldsymbol{\sigma_T}$ the overall stress tensor, $\boldsymbol{\sigma_E}$ and $\mathcal{E}(\boldsymbol{u})$ the effective stress and strain tensors and $\boldsymbol{C}$ the macroscopic elastic modulus. To summarize we need to solve the fully coupled system composed of (5.3) – (5.4) together with (2.18) and (5.1).

The above approach consists of a first step towards the construction of a coupled hydro-mechanical model in the shale matrix. Following the guidelines of our earlier work [28, 29] the coupling with flow and deformation in the hydraulic fractures can be pursued within the context of the DFM (discrete fracture model) where the fracture network is treated in a discrete fashion playing the role of interface conditions for flow in the matrix. Alternative more denser networks of natural fractures can also be incorporated in the current framework by exploring the double porosity models for deformable media discussed in [6, 9, 10, 37].

6. Conclusion

In this paper we developed a new adjoint–based optimization procedure seated on a new model of methane withdrawal in shale gas reservoirs. A preliminary version of the forward model was constructed seated on a time–scale assumption of fast flow in the network of hydraulic fractures compared to the matrix. In this scenario a new nonlinear pressure equation was constructed where constitutive laws for the effective parameters (retardation coefficient and hydraulic conductivity) were developed strongly correlated with microstructure response. A new constitutive law for the retardation coefficient parametrized by the TOC provided new insight into the local physics of the problem which is transferred to the subsequent optimization procedure. In this context we pursued to minimize a family of cost functions parametrized

by a power law exponent β which reproduces degenerated cases of cumulative gas production and an energy-based function for extreme values of β. In addition, weight functions in time were also included in the objective function to incorporate corrections due to variable cash–flow and discount rates leading to a different characterization based on the net present value. A new adjoint problem was constructed to compute the sensitivity of the objective function with perturbations in the control variable given by the pressure (or density) in the well/fracture. Numerical results illustrated the optimal controlled density decline trajectories in time. By identifying the objective function with a NPV–based function remarkable alternative smoother decline paths in time were constructed showing improvement in profits considering input data extracted from Marcellus and Barnett formations. To the authors best knowledge the framework proposal herein is a first attempt towards the construction of a robust optimization framework for gas flow in low permeable shale formations. Subsequent developments will focus on the coupled matrix/fracture hydrodynamics with fractures treated as lower $(n-1)$–dimensional objects.

REFERENCES

[1] Akkutlu, I. Y., Fathi E., Multiscale gas transport in shales with local kerogen heterogeneities. *SPE journal*, **17**(04), 1002-1011 (2012).

[2] Akkutlu, I. Y., Efendiev, Y., Savatorova, V., Multi–scale asymptotic analysis of gas transport in shales matrix. *Transport in Porous Media*, **107**(1), 235–260 (2015).

[3] Auriault, J. L., Boutin C., Geindreau C., Homogenization of coupled phenomena in heterogeneous media. *John Wiley - Sons*, Inc (2009).

[4] Bazaraa M. S., Sherali H. D. and Shetty C. M., Nonlinear programming. *John Wiley & Sons* (2006).

[5] Bicheng Y., Yuhe W., John E. K., Beyond dual-porosity modeling for the simulation of complex flow mechanisms in shale reservoirs. *Society of Petroleum Engineers*, SPE Reservoir Simulation Symposium, 18-20 February, The Woodlands, Texas, USA (2013).

[6] Borja, R.I., Choo, J., A constitutive framework for porous materials with evolving internal structure. *Computer Methods in Applied Mechanics and Engineering*, Vol. 309, 653–679 (2016).

[7] Choi K. K. and Kim N. H., Structural sensitivity analysis and optimization 1: Linear systems. *Springer* (2005).

[8] Choi K. K. and Kim N. H., Structural sensitivity analysis and optimization 2: Nonlinear systems and applications. *Springer* (2005).

[9] Choo, J., Borja, R.I., Stabilized mixed finite elements for deformable porous media with double porosity. *Computer Methods in Applied Mechanics and Engineering*, Vol. 293, 131–154 (2015).

[10] Choo, J., Joshua A. White, and Borja, R.I., Hydromechanical Modeling of Unsaturated Flow in Double Porosity Media. *International Journal of Geomechanics*, Vol. 16(6) (2016).

[11] Christopher R. C., Morteza N., Danial K., Turgay E., Production analysis of tight-gas and shale-gas reservoirs using the dynamic-slippage concept. *SPE journal*, **17**(01), 230-242 (2012).

[12] Collin M., Rasmuson A., A comparison of gas diffusivity models for unsaturated porous media. *Soil Sci. Soc. Am. J*, **52**, 1559-1565 (1988).

[13] Coussy, O., *Poromechanics*, John Wiley & Sons, 2004.

[14] Curtis M. E., Cardott B. J., Sondergeld C. H., Rai C. S., Development of organic porosity in the Woodford Shale with increasing thermal maturity. *International Journal of Coal Geology*, **103**, 26-31 (2012).

[15] Curtis M. E., Sondergeld C. H., Rai C. S., Relationship between organic shale microstructure and hydrocarbon generation. *Unconventional Resources Conference-SPE*, The Woodlands, Texas (2013).

[16] Curtis M. E., Sondergeld C. H., Rai C. S., Investigation of the Microstructure of Shales in the Oil Window. *Unconventional Resources Technology Conference, Denver, Colorado, USA*, 12-14 August (2013).

[17] Dong L., Peng Y., Hongmei L., Tian L., Daoyong T., Weiwei Y., Hongping H., High-pressure adsorption of methane on montmorillonite, kaolinite and illite. *Applied Clay Science*, **85**, 25-30 (2013).

[18] Freeman, C.M., Moridis, G.J., Blasingame, T.A., A Numerical Study of Microscale Flow Behavior in Tight Gas and Shale Gas Reservoir Systems. *Transport in Porous Media*, **90(1)**, 253-268 (2011).

[19] Frih N., Roberts J. E., Saada A., Modeling fractures as interfaces: a model for Forchheimer fractures. *Computational Geosciences*, **12**, 91-104 (2008).

[20] Ghassemzadeh, J., Xu, L., Tsotsis, T. T., and Sahimi, M., Statistical Mechanics and Molecular Simulation of Adsorption in Microporous Materials: Pillared Clays and Carbon Molecular Sieve Membrane, *J. Phys. Chem. B*, **104**, 16, 3892–3905 (2000).

[21] Gill P.E., Murray, W. and Wright M. H., Practical Optimization. *Elsevier Academic Press* (1981).

[22] Haug E. J., Choi K. K. and Komkov V., Desing sensitivity analysis of structural systems. *Academic Press* (1986).

[23] Islam M. R., Unconventional gas reservoirs: evaluation, appraisal, and development. *Gulf Professional Publishing* (2014).

[24] Jahne, B., Heinz, G., Dietrich, W., Measurement of the diffusion coefficients of sparingly soluble gases in water. *Journal of Geophysical Research*, Vol 92, C10, 10767–10776, (1987).

[25] Javadpour, F., Nanopores and apparent permeability of gas flow in mudrocks (shale and siltstone), *J. Can. Petrol. Technol.*, **48**(8), 16–21 (2009).

[26] Jin, Z. and Firoozabadi, A., Methane and Carbon Dioxide Adsorption in Clay–Like Slit Pores by Monte Carlo Simulations, *Fluid Phase Equilibria*, **360**, 456–465 (2013).
[27] Kierlik E., Rosinberg M. L., Density-functional theory for inhomogeneous fluids : Adsorption of binary mixtures. *Physical Review A*, **44**, 5025-5037 (1991).
[28] Le T. D., Murad A. M., Pereira A. P., Boutin C., Bridging between macroscopic behavior of shale gas reservoirs and confined fluids in nanopores. *Computational Geosciences*, **20**, 751-771 (2016).
[29] Le T. D., Murad A. M., Pereira A. P., A New Matrix/Fracture Multiscale Coupled Model for Flow in Shale Gas Reservoirs. *SPE journal*,22(1), 265–288 (2016).
[30] Liming J., Tongwei Z., Kitty L. M., Junli Q., Xiaolong Z., Experimental investigation of main controls to methane adsorption in clay-rich rocks. *Applied Geochemistry*, **27**, 2533-2545 (2012).
[31] Luenberger D. G. and Ye Y., Linear and Nonlinear Programming. *Springer* (2008).
[32] Mason, E. A., Malinauskas A. P., Gas transport in porous media: the dusty-gas model. *Elsevier Science* (1983).
[33] Monteiro, P. J. M., Rycroft, C. H., and Barenblatt, G. I., A mathematical model of fluid and gas flow in nanoporous media. *Proceedings of the National Academy of Sciences of the United States of America*, **109(50)**, 20309–20313 (2012).
[34] Mehmani, A., Prodanovic, M., Javadpour, F., Multiscale, multiphysics network modeling of shale matrix gas flows, *Transport in Porous Media*, **99**), 377–390 (2013).
[35] Prausnitz, John M. and Lichtenthaler, Rudiger N. and de Azevedo, Edmundo G., Molecular thermodynamics of fluid-phase equilibria. Prentice Hall (1998).
[36] Ranjbar, E., and Hassanzadeh, H., Matrix–fracture transfer shape factor for modeling flow of a compressible fluid in dual–porosity media. *Advances in Water Resources*, **34**, 627–639 (2011).
[37] Rocha, A. C., Murad, M. A., and Le, T. D., A new model for flow in shale-gas reservoirs including natural and hydraulic fractures. *Computational Geosciences*, **21**, Issue 5–6, pp 1095–1117 (2017).
[38] Rosenfeld Y., Free-energy model for the inhomogeneous hard-sphere fluid mixture and densityfunctional theory of freezing. *Physical Review Letters*, **63**(09), 980-983 (1989).
[39] Ross D. J. K., Bustin R. M., The importance of shale composition and pore structure upon gas storage potential of shale gas reservoirs. *Marine and Petroleum Geology*, **26**, 916-927 (2009).
[40] Sakhaee-Pour A., Bryant S., Gas Permeability of Shale. *Society of Petroleum Engineers*, **15**, issue 04 (2012).
[41] Segura, C. J., Vakarin, E. V., Chapman, W. G. and Holovko, M. F., A comparison of density funcional and integral equations theories vs Monte Carlo simulations for hard sphere associating fluids near a hard wall, *J. Chem. Phys.*, **108**, 4837 (1998).
[42] Smith M. B., Montgomery C. T., Hydraulic Fracturing (Emerging Trends and Technologies in Petroleum Engineering). *CRC Press* (2015).
[43] Yu W. and Sepehrnoori K., Optimization of Multiple Hydraulically Fractured Horizontal Wells in Unconventional Gas Reservoirs. *Journal of Petroleum Engineering* (2013).
[44] Yu W., Sepehrnoori K., Tadeusz W. P., Evaluation of gas adsorption in Marcellus shale. *Society of petroleum engineers*, SPE Annual Technical Conference and Exhibition, 27-29 October, Amsterdam, The Netherlands (2014).
[45] Yu W. and Sepehrnoori K., Simulation of gas desorption and geomechanics effects for unconventional gas reservoirs. *Fuel*, **116**, 455-464 (2014).
[46] Yan, B., Wang, Y. and Killough, J. E., Beyond Dual-Porosity Modeling for the Simulation of Complex Flow Mechanisms in Shale Reservoirs. SPE Reservoir Simulation Symposium, The Woodlands, Texas, 18–20 February, SPE-163651-MS, http://dx.doi.org/10.2118/163651-MS (2013).
[47] Xia, L., and Luo, D., A method for calculating economic critical depth of shale gas resources in China via break-even analysis. *Journal of Natural Gas Science and Engineering*, **21**, 1091–1098 (2014).
[48] Zhehui J., Abbas F., Methane and carbon dioxide adsorption in clay-like slit pores by Monte Carlo simulations. *Fluid Phase Equilibria*, **360**, 456-465 (2013).
[49] Zimmerman, R.W., Chen, D.-W., Cook, N.G.W. , The effect of contact area on the permeability of fractures, *Journal of Hydrology*, Vol. 139, **1–4**, 79–96 (1992).

APPENDIX A. DEPENDENCE OF THE RETARDATION COEFFICIENT ON TOC

In what follows we develop a direct relation between the volume fractions φ_k and TOC. Denoting M_K and M_I the mass of the kerogen and inorganic matter, ρ_K and ρ_I the corresponding densities we have by definition

$$\rho_K := \frac{M_K}{V_K^s} \qquad , \qquad \rho_I := \frac{M_I}{V_I}, \tag{A.1}$$

where V_K^s and V_I are the volumes occupied by the solid within the organic aggregates and the inert inorganic matter respectively. The total organic carbon TOC is defined by

$$TOC := \frac{M_K}{M_K + M_I} \tag{A.2}$$

Thus denoting V_P and V_K the volume occupied by the interparticle pores and the kerogen aggregates with $V_T = V_P + V_K + V_I$ we have

$$\varphi_P := \frac{V_P}{V_T} \qquad , \qquad \varphi_K := \frac{V_K}{V_T} \qquad \text{and} \qquad \varphi_I := \frac{V_I}{V_T}, \tag{A.3}$$

where φ_P, φ_K φ_I are the volume fractions of the interparticle pores, kerogen aggregates and inorganic matter, respectively. We then have

$$\begin{aligned} 1 - \varphi_I = 1 - \frac{V_I}{V_T} = 1 - \left(\frac{V_I}{V_I + V_K}\right)\left(\frac{V_I + V_K}{V_T}\right) = 1 - \left(\frac{V_I}{V_I + V_K}\right)\left(\frac{V_T - V_P}{V_T}\right) = \\ = 1 - \left(\frac{V_I}{V_I + V_K}\right)(1 - \varphi_P) = 1 - \left(1 - \frac{V_K}{V_I + V_K}\right)(1 - \varphi_P) = 1 - (1 - \phi_S^o)(1 - \varphi_P), \end{aligned} \tag{A.4}$$

where ϕ_S^o the volume fraction of the organic matter in the solid phase given by

$$\phi_S^o := \frac{V_K}{V_I + V_K} = \frac{1}{1 + \dfrac{V_I}{V_K}} = \frac{1}{1 + \dfrac{V_I V_K^s}{V_K V_K^s}}. \tag{A.5}$$

Moreover, the intrakerogen aggregates nanoporosity ϕ_N is defined in the form

$$\phi_N := \frac{V_K - V_K^s}{V_K} \qquad \Leftrightarrow \qquad 1 - \phi_N = \frac{V_K^s}{V_K}. \tag{A.6}$$

Combining the expressions (A.5) and (A.6) we have

$$\phi_S^o = \frac{1}{1 + (1 - \phi_N)\dfrac{V_I}{V_K^s}}. \tag{A.7}$$

Also, from the expressions (A.1) we obtain

$$\frac{V_I}{V_K^s} = \frac{\rho_K M_I}{\rho_I M_K} \qquad \text{and} \qquad \frac{M_I}{M_K} = \frac{1 - \dfrac{M_I}{M_I + M_K}}{\dfrac{M_K}{M_I + M_K}} = \frac{1 - TOC}{TOC}. \tag{A.8}$$

Replacing (A.8) in (A.7) gives

$$\phi_S^o = \frac{1}{1 + \dfrac{\rho_K(1 - TOC)}{\rho_I TOC}(1 - \phi_N)}.$$

Finally, replacing the above expression in (A.4) we obtain the dependence for the volume fractions of the kerogen aggregates on the TOC in the form

$$\varphi_K = 1 - \varphi_P - \varphi_I = \frac{1 - \varphi_P}{1 + \dfrac{\rho_K(1 - TOC)}{\rho_I TOC}(1 - \phi_n)}. \tag{A.9}$$

(A.A. Novotny) LABORATÓRIO NACIONAL DE COMPUTAÇÃO CIENTÍFICA LNCC/MCT, COORDENAÇÃO DE MATEMÁTICA APLICADA E COMPUTACIONAL, AV. GETÚLIO VARGAS 333, 25651-075 PETRÓPOLIS - RJ, BRASIL
E-mail address: novotny@lncc.br

(M. Murad) LABORATÓRIO NACIONAL DE COMPUTAÇÃO CIENTÍFICA LNCC/MCT, COORDENAÇÃO DE MATEMÁTICA APLICADA E COMPUTACIONAL, AV. GETÚLIO VARGAS 333, 25651-075 PETRÓPOLIS - RJ, BRASIL
E-mail address: murad@lncc.br

(S. Lima) UNIVERSIDADE FEDERAL DO RIO GRANDE DO NORTE UFRN/MEC, AV. SALGADO FILHO, S/N, LAGOA NOVA, 59078–970, NATAL, RN, BRAZIL
E-mail address: sidarta@ccet.ufrn.br